Three-dimensional cellular automaton modeling of silicon crystallization with grains in twin relationships

Adrian Pineau, Gildas Guillemot, Guillaume Reinhart, Gabrielle Regula, Nathalie Mangelinck-Noël, Charles-André Gandin

Three-dimensional cellular automaton modeling of silicon crystallization with grains in twin relationships

A. Pineau[a], G. Guillemot[a], G. Reinhart[b], G. Regula[b], N. Mangelinck-Noël[b], Ch.-A. Gandin[a,*]

[a] MINES ParisTech, PSL Research University, CEMEF UMR CNRS 7635, CS10207, 06904 Sophia Antipolis, France
[b] Aix Marseille Univ., Université de Toulon, CNRS, IM2NP, Marseille, France

A B S T R A C T

A three-dimensional model is proposed to simulate the grain structure in directionally solidified silicon. This includes the nucleation and growth of grains in twin relationship whose formation is very frequent during silicon solidification. Based on analyses of in-situ and real-time observations of the crystallization front, a three-dimensional cellular automaton method is developed to model the dynamic of {111} facets, groove formation at grain boundaries, nucleation and growth of grains in twin relationship. The model is applied to well-characterized experiments assuming the frozen temperature approximation. A comparison of solidification sequences, crystallographic orientation maps, and coincidence site lattice maps in both experiment and simulation results is achieved. Results demonstrate that the model could be applied to optimize crystallization processes for both polycrystalline and cast-mono silicon fabrication processes.

1. Introduction

Industrial photovoltaic panels are mainly based on the use of silicon material. Crystalline silicon has the largest market share due to: the availability of the raw material, its non-toxicity, efficiency and high level of technology readiness [1]. The photoelectric properties of the solar cells are strongly linked to the production chain, including purity of the raw material, crystallization, wafering, cell processing, and module integration. During crystallization, the grain structure and associated defects are generated, defining the grain size, the defect density (e.g., dislocations), the crystallographic orientation distribution, twin-relationships and distribution of impurities. The crystallization features need to be controlled in order to optimize final electrical properties because they can act as recombination centers of charge carriers, thus lowering the efficiency of the photoelectric panels [2–5]. Research and development efforts include the study of new methods using seeding [6] in classical directional solidification processes used in the industry to produce multi-crystalline silicon.

During the manufacturing of silicon ingots in crucibles, twin grain boundaries are commonly observed in any solidification process and strongly influence the final grain structure. Voigt *et al.* [7,8] analyzed the orientation of each grain on a $5 \times 5\,cm^2$ wafer. They observed that most of the grains are in twin relationship and more than 50% of the grain boundaries correspond to $\Sigma 3$, $\Sigma 9$, $\Sigma 27$ and $\Sigma 81$ twins boundaries. The most common twins in silicon are of $\Sigma 3$ type and can be described as an odd number of 60° rotation of the crystal lattice around a ⟨111⟩ direction. Hence, new grains in $\Sigma 3$ relationship nucleate on {111} planes [3], their formation being enhanced by the low energy needed for twinning process [9]. Jackson [10] proposed a criterion aiming at predicting the morphology of the solidification front that can be applied to silicon to identify the faceted growth orientations. The Jackson criterion is based on the parameter $\alpha = (\eta/Z)(L/k_B T_M)$, where η is the number of nearest neighbor sites adjacent to an atom in the plane of the solid-liquid (s/l) interface, Z is the total number of nearest neighbors of an atom in the crystal, L is the latent heat of fusion, T_M is the melting temperature of the material and k_B is the Boltzmann constant. If α is higher than a critical value equal to 2, the s/l interface is faceted, and rough otherwise. In the case of pure silicon, α is equal to 2.7 for {111} growth planes and lower than 2 for all other planes. Therefore, it indicates that growing facets are solely {111} planes in silicon. Being coherent boundaries, $\Sigma 3$ twins exhibit no dangling bonds and do not directly lower the final efficiency of solar cells [11]. However, the nucleation of a grain in $\Sigma 3$ twin relationship can be at the origin of the formation of higher order incoherent, symmetric or asymmetric twin boundaries such as $\Sigma 9$ or $\Sigma 27$ by competition [12] and hence responsible for dislocation emission [3,13], impurity segregation and electron-holes pair recombination degrading the photoelectric properties.

To be able to control the formation of the grain structure and of the defects during the solidification process, it is essential to understand the dynamics of grain nucleation, growth and competition. In the last few years, the GaTSBI (Growth at high Temperature observed by Synchrotron Beam Imaging) device dedicated to the characterization of silicon solidification from the melt using synchrotron in-situ X-ray imaging has been developed [14,15]. The authors use two

complementary techniques: X-ray radiography to observe the morphology of the s/l interface, e.g. {111} facets, and X-ray topography giving access to crystallographic orientations of grains as well as possible presence of plane bending due to local strain fields induced by defects formed in the sample during growth.

Various numerical methods have been used to model polycrystalline silicon growth during directional solidification. Lan and co-authors [16,17] have performed three-dimensional (3D) phase field computations considering highly anisotropic interfacial energy and kinetic coefficients. They evidenced the formation of {111} faceted interfaces at the grain boundaries during growth as commonly observed experimentally. Miller *et al.* [18] also performed phase field computations for a bicrystal in a two-dimensional (2D) domain. The grain boundary behavior was found to highly rely on the crystallographic orientations of the two neighboring grains in competition. Despite being the most advanced method for modeling of phase boundaries created by impingement of s/l interfaces, the phase field approach is computationally intensive. As a consequence, no simulations have been reported yet for practical applications, i.e. for simulation of a grain structure representative of a casting process. Nadri *et al.* [19] developed a two-dimensional model aiming at predicting the columnar grain structure evolution along a polycrystalline silicon ingot. This approach considers random nucleation at the bottom of the crucible, grain boundary formation due to the presence of grooves at the s/l interface, as well as growth and twinning events. Although the model is able to give a general tendency, its 2D approximation prevents any quantitative comparison with experimental observations in particular as concern the grain crystallographic orientation. Wu *et al.* [20] used a model designed for 3D simulations of dendritic grain structures in metallic alloys by means of a Cellular Automaton (CA) method. So neither the kinetics of the s/l interface, nor the development of {111} facets and nucleation of grains in twin relationship on these facets were accounted for. Recently, Qi *et al.* [21] also proposed a CA method to compute the development of grains using input data obtained from phase field microscopic simulations. This new method was able to satisfactorily reproduce experimental observations [12] and demonstrated the efficiency of the CA approach although the domain size was limited and the simulations were restricted to 2D. Thus, a model is still missing for addressing the grain structure formed upon silicon crystallization at the scale of the process.

CA aims at modeling complex phenomena through the use of local simple laws. These laws define the evolution of state and properties of cells, the latter being the unit polyhedron of a regular lattice that entirely paves the region of interest. They depend upon their surrounding environment, e.g. states and properties within nearby cells. CA modeling of grain boundary formed upon solidification of dendritic grains was proposed by Gandin and Rappaz [22]. This method simulates the development of grain envelopes rather than the full dendritic microstructure, with the advantage to be applicable for large simulation domains. This is necessary as the development of the grain structure is strongly dependent on phenomena taking place at large distances, such as recalescence [22,23], melt convection [24], transport of the equiaxed dendritic grains [25], macrosegregation [26–30]; all being influenced by time-dependent boundary conditions applying on complex casting geometries. In turn, the development of the grain structure strongly influences heat and mass transfers at the scale of the casting. Coupling of the CA method with a solution of the average conservation equations solved at the scale of the casting using the finite element (FE) method was thus achieved, leading to the so-called CA-FE model. Lastly, the CA method was extended to 3D for quantitative description of the crystal orientation [31–33]. It was applied to compute multiple pass welding grain structures [34,35] and is currently developed for application to additive manufacturing [36–38].

The present work aims at modeling silicon growth upon directional solidification using the 3D CA method. In-situ experimental observations during growth showing faceted interfaces, successive twinning and grain nucleation [3,4] are first introduced. Their description is at the basis of the developments of the CA algorithms so as to reproduce {111} facets growth and nucleation of grains in twin relationship. Comparisons with in-situ experimental observations and post-mortem characterizations by EBSD (Electron Back Scattered Diffraction) analyses are then presented. Due to the well-defined heat flow conditions of the experimental set-up, the frozen temperature approximation is adopted. Results are discussed to better outline the model capabilities and the basic phenomena leading to formation of grains in twin relationship upon silicon crystallization.

2. Experimental

The GaTSBI experimental device is briefly described hereafter. This equipment is dedicated to solidification studies of high temperature materials using synchrotron in-situ X-ray radiography and topography [14,15]. Typical radiographs are displayed in Figures 1 and 2. To obtain these images, a monocrystalline silicon sample is placed in a two resistive heaters furnace. The sample is first partially melted by increasing the temperature of the upper and bottom heaters up to 1719 K and 1566 K, respectively. This temperature difference imposes a constant temperature gradient of the order of 3000 K m^{-1}. A cooling rate is then applied on both heaters to trigger and control the solidification speed. During the melting and solidification steps, the sample is crossed by an X-ray synchrotron beam. Two imaging modes are used: radiography based on density differences between the solid and liquid phases to produce absorption based-contrasted images and diffraction (historically named topography). During solidification, several grains nucleate as described in details in reference 3. They compete to form the final grain structure. The interaction of the different grains creates grain boundaries. Fig. 1 shows magnified regions around grain boundary grooves formed at the encounter of s/l interfaces of the grains.

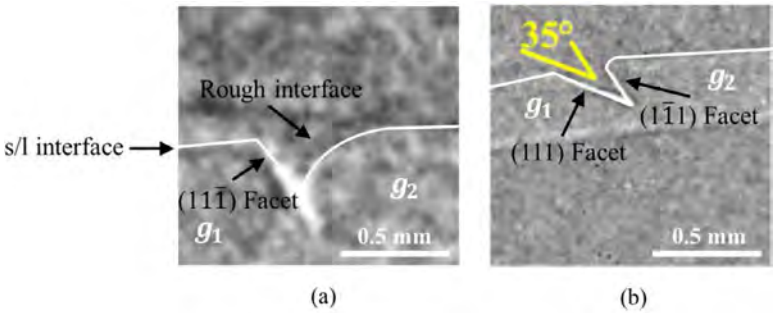

Fig. 1. X-ray radiography images during solidification of a silicon sample using the GaTSBI experimental device [14,15] revealing (a) rough/faceted and (b) faceted/faceted grain boundary grooves with (a) temperature gradient $G = 2200$ K m^{-1}, cooling rate $\dot{T} = -0.003$ K s^{-1}, Euler angles of the LHS grain, $g_1 = (223.8^\circ, 28.3^\circ, 15.3^\circ)$, and of the RHS grain, $g_2 = (95.1^\circ, 48.3^\circ, 62.1^\circ)$, and (b) $G = 1200$ K m^{-1}, $\dot{T} = -0.016$ K s^{-1}, $g_1 = (17.6^\circ, 88.3^\circ, -43.4^\circ)$ and $g_2 = (-21.3^\circ, 89.7^\circ, 47.3^\circ)$.

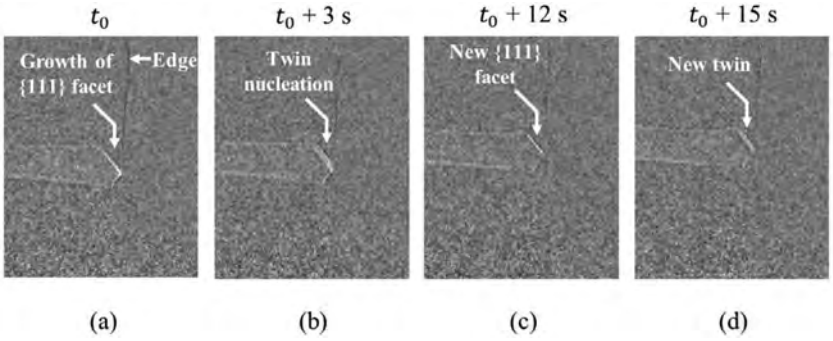

Fig. 2. X-ray radiography images as part of a time sequence during solidification of a silicon sample revealing (a, c) faceted growth and (b, d) twin nucleation at the sample edge. Temperature gradient: 1200 K m^{-1}, cooling rate –0.016 K s^{-1}, Euler angles of the seed, $g = (356^\circ, 44^\circ, 3^\circ)$.

The groove or shape of the undercooled s/l interface morphologies depend on the relative crystallographic orientation of the neighboring grains. Three morphologies are described between grains according to Duffar *et al.* [39]: rough/rough, rough/faceted and faceted/faceted. Rough/faceted grain boundary grooves were observed experimentally by X-ray radiography during silicon crystallization as illustrated in Fig. 1(a) [3,40]. Faceted/faceted grooves were observed by an optical imaging method by Hu *et al.* [41] and by X-ray imaging [40,42]. Fig. 1(b) shows a faceted/faceted grain boundary groove during growth in an experiment described in reference [42] with prescribed temperature gradient between heaters, 3000 K m^{-1}, cooling rate on both heaters, –0.016 K s^{-1}, [001] seed orientation in the solidification direction, and [110] and [1$\bar{1}$0] orientations normally and transversally to the sample, respectively. During this experiment, the measured local temperature gradient was 1200 K m^{-1} [3]. At mold walls and edges, {111} facets can also be observed and have a projection on the radiography related to the orientation of the {111} plane as can be seen in Fig. 2.

As in other experiments characterized by X-ray imaging, several twin grains nucleate on {111} facets after growth starts from the pristine seed. Such nucleation of a twin on a {111} facet at the edge of the sample is observed in Fig. 2. These nucleation events are repeated successively during growth on the {111} facets. The nucleated grains enter in competition together with the grain from the pristine seed and form the final grain structure as can be seen in Figure 3. The later displays four maps extracted from EBSD measurements performed in a scanning electronic microscope on the sample after solidification. Fig. 3(a), (b) and (c) are grain structure maps represented with the Inverse Pole Figure (IPF) color code using the longitudinal, *x* (also growth direction), transverse, *y*, and normal, *z*, directions of the sample, respectively. Fig. 3(d) is the Coincidence Site Lattice (CSL) map revealing the grain boundary type and the twin relationships. $\Sigma 3$ boundaries correspond to twins on {111} facets with a rotation of an odd number of 60° about the normal to the facet. According to the in-situ observation compared to the final grain structure, they are the only twin boundaries formed by nucleation of new twin grains, the other twin boundaries (e.g., $\Sigma 9$ and $\Sigma 27$) being only formed by growth competition. The nucleation temperatures at the bottom of faceted/faceted grain boundary grooves and at the bottom of edge facets were estimated. Values of undercooling lower than 1 K were measured at both faceted/faceted grooves and edge facet bottom, the undercooling at the edge facets being higher than in the grain boundary grooves [42].

3. Modeling

The description of the CA model and its extension for direct simulation of a polycrystalline silicon structure is given hereafter, including the nucleation and growth of grains in twin relationship. The basics of the CA growth and capture algorithms are first recalled. New algorithms for activation and growth of facets, followed by nucleation and growth of grains in twin relationship, are then

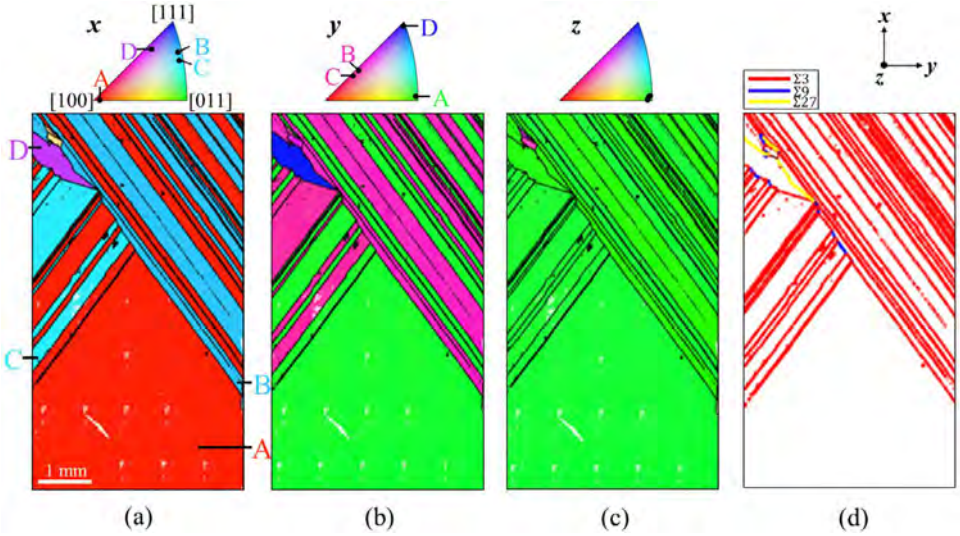

Fig. 3. Grain structure maps for a directionally solidified silicon sample obtained by EBSD analyses [4]. The (a) longitudinal direction of the sample, **x** (also growth direction), (b) transverse direction of the sample, **y**, and (c) normal direction to the sample, **z**, are projected in the frame made of the measured {[100], [010], [111]} crystallographic directions and represented using the color code of the IPF. The CSL map characterizing the grain boundary relationships is shown in (d) with twin boundaries $\Sigma 3$, $\Sigma 9$ and $\Sigma 27$ appearing in red, blue and yellow, respectively. Temperature gradient: 1200 K m^{-1}, cooling rate –0.016 K s^{-1}, Euler angles of the seed, $g = (356^\circ, 44^\circ, 3^\circ)$.

introduced. The 3D model is available and has been used for the simulations. For the sake of simplicity, the figures are yet presented in 2D.

3.1. CA grid and indexes

The cellular automaton method used in the present model is based on a regular lattice of square (2D) or cubic (3D) cells with a constant size, l_{CA}. The lattice covers the whole simulation domain and constitutes the CA grid. Each cell ν is uniquely defined by its coordinate center, $C_\nu(x_\nu, y_\nu)$ ($C_\nu(x_\nu, y_\nu, z_\nu)$ in 3D), and two indexes I_ν and I_ν^g. Index I_ν describes the cell state. In the present model, cells are liquid, $I_\nu = 0$, or belongs to the microstructure as a consequence of a nucleation or capture events, $I_\nu = 1$. The grain index of cell ν, I_ν^g, indicates the grain number to which it belongs to, i.e. $I_\nu^g = g$. Crystallographic orientations of grains are described by angles, ϕ in 2D and (ϕ_1, ϕ, ϕ_2) in 3D using the Euler angles with the Bunge convention [43]. For silicon crystals, they represent rotation angles defining the ⟨10⟩ crystallographic directions from a reference frame attached to the sample (⟨100⟩ in 3D). Note that in a 2D approximation, the ⟨10⟩ crystallographic directions lie in the reference frame so a single rotation angle ϕ is sufficient.

3.2. CA growth and capture algorithms

Figure 4 illustrates the main growth and capture algorithms used by the cellular automaton method [33]. Each cell ν having at least one neighboring liquid cell is associated with a quadrangle with diagonals representing its four ⟨10⟩ directions (six ⟨100⟩ in 3D). In Fig. 4 the quadrangle is a simple square (a regular octahedron in 3D). Growth of the diagonals is computed by integration over time of a growth kinetic law that is either related to experimental measurements or to theories. For instance, in case of dendritic microstructures [44], a dendrite tip growth kinetic model is well established and could be fitted by a simple power law between the velocity along the ⟨10⟩ directions, $v_\nu^{\langle 10\rangle}$ ($v_\nu^{\langle 100\rangle}$ along ⟨100⟩ directions in 3D), and the tip undercooling [44], ΔT, the latter defined by the difference between the melting point of the material, T_M, and the tip temperature, T. For silicon growth [45], a linear law is appropriate. Experimental observations, within the spatial resolution of the set-up, also show that the rough part of the solidification front growing directionally remains smooth, grooves solely locally destabilizing the s/l interface due to the presence of {111} facets [42]. This means that the grains defining the directionally solidifying s/l interface grow with the same stationary undercooling being independent of the crystal orientation. To reproduce these observations, the following form of the growth kinetics along ⟨10⟩ directions (⟨100⟩ in 3D) is proposed:

$$v = (A\ /cos\ \alpha)\ \Delta T \tag{1}$$

where A is a measured growth kinetics parameter [42]. Angle α denotes the misorientation between the best aligned ⟨10⟩ direction of the grain (⟨100⟩ in 3D) and the temperature gradient. Thus, for a given isotherm velocity v_L, the stationary undercooling of a grain with crystallographic orientations characterized by misorientation α reaches undercooling ΔT, i.e. a unique value for all grains whatever its orientation. With this methodology, for a given undercooling and when stationary growth is achieved, the s/l interface made of an assembly of grains with different crystallographic orientation defines a planar front. Applied to a growing cell ν along ⟨10⟩ directions (⟨100⟩ in 3D), Eq. (1) computes velocity $v_\nu^{\langle 10\rangle}$ ($v_\nu^{\langle 100\rangle}$ in 3D) using the temperature T_ν estimated at the cell center C_ν.

The origin of the ⟨10⟩ directions (⟨100⟩ in 3D) coincides with the growing center, G_ν, defined at the time of capture of cell ν. Joining the four vertices $S_\nu^{\langle 10\rangle}$ (six $S_\nu^{\langle 100\rangle}$ in 3D) defines a quadrangle or growth envelope centered in G_ν (blue quadrangles in Fig. 4). Upon growth from time t to time $t + \Delta t$, the $S_\nu^{[01]}S_\nu^{[10]}$ side of the $S_\nu^{\langle 10\rangle}$ quadrangle (a triangular surface joining three adjacent $S_\nu^{\langle 100\rangle}$ directions in 3D) encompasses the center of the liquid cell μ ($I_\mu = 0$) as sketched in Fig. 4(a). The cell μ is thus captured and its state index is switched to $I_\mu = 1$ so as to permit its growth and further propagation of the grain envelope to the neighboring liquid cells. A growth center G_μ and vertices $S_\mu^{\langle 10\rangle}$ ($S_\mu^{\langle 100\rangle}$ in 3D) are then initialized, defining a quadrangle (octahedron in 3D) for the cell μ. This is achieved by a homothetic transformation of quadrangle $S_\nu^{\langle 10\rangle}$ ($S_\nu^{\langle 100\rangle}$ in 3D) at the time of capture, $t + \Delta t$. The closest $S_\nu^{\langle 10\rangle}$ ($S_\nu^{\langle 100\rangle}$ in 3D) vertex to the projection of the cell center C_μ onto the capturing side is identified and coincides with its corresponding $S_\mu^{\langle 10\rangle}$ ($S_\mu^{\langle 100\rangle}$ in 3D) vertex ($S_\mu^{[01]} = S_\nu^{[01]}$ in Fig. 4(b)). The homothetic ratio is lower than unity. Its value is defined so as to keep the growth center G_μ close to the cell center C_μ and to prevent overly large growth envelopes. Finally, the Moore environment is used to define the cell neighborhood, i.e. using the eight nearest neighboring cells [44].

3.3. Facets activation and growth

The new algorithm to initiate and grow {11} facets ({111} in 3D) is now described. Four facets (eight in 3D) are defined for each grain g and tracked with virtual planes using Cartesian equations $D_g^{\{11\}} : a_g^{\{11\}}x + b_g^{\{11\}}y + c_g^{\{11\}} = 0$ ($D_g^{\{111\}} : a_g^{\{111\}}x + b_g^{\{111\}}y + c_g^{\{111\}}z + d_g^{\{111\}} = 0$ in 3D). An activation undercooling, $\Delta T_g^{\{11\}}$ ($\Delta T_g^{\{111\}}$ in 3D), is associated to each

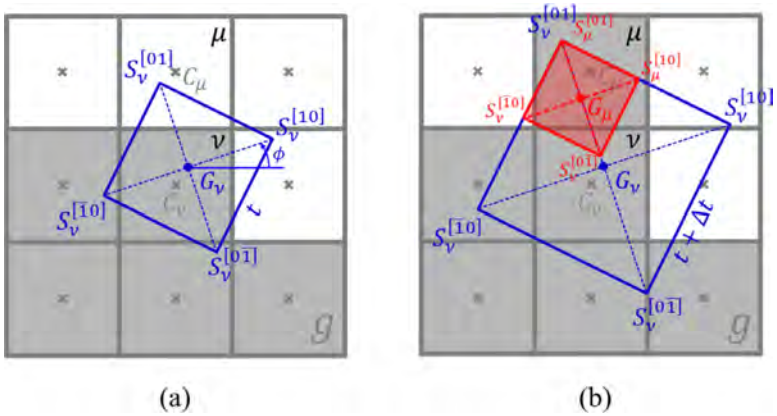

Fig. 4. Schematics of (a) the two-dimensional standard cellular automaton growth algorithm for cell ν centered in C_ν and (b) the capture algorithm for cell μ centered in C_μ, showing (blue) quadrangles delimited by the four $S_\nu^{\langle 10\rangle}$ vertices associated to the growth envelope centered in G_ν at time t and $t + \Delta t$, (red) the location of the newly initialized growth center G_μ and its vertices $S_\mu^{\langle 10\rangle}$, (grey colored) captured cells and (white colored) liquid cells. All captured cells belong to the same grain g defined by the orientation angle ϕ and the same value of the grain index. Only the quadrangle associated to cell ν is sketched while all captured cells with at least one neighboring liquid cell have similar growing quadrangles.

plane. Its value is randomly chosen using a given normal distribution law of mean value $\Delta T_{g,m}^{\{11\}}$ and standard deviation $\Delta T_{g,s}^{\{11\}}$ ($\Delta T_{g,m}^{\{111\}}$ and $\Delta T_{g,s}^{\{111\}}$ in 3D). The choice of the mean value and standard deviation is detailed in the results section.

3.3.1. *Facet activation*

Upon capture of cell μ by the growing cell ν belonging to grain g (Fig. 4), its undercooling ΔT_μ is computed. It is compared to the activation undercooling of each {11} plane ({111} in 3D) leading to faceted growth for grain g, $\Delta T_g^{\{11\}}$ ($\Delta T_g^{\{111\}}$ in 3D). The condition to activate one of the facets is simply $\Delta T_\mu < \Delta T_g^{\{11\}}$ ($\Delta T_\mu < \Delta T_g^{\{111\}}$ in 3D). However, not all {11} facets ({111} in 3D) can develop. This is illustrated in Figure 5 with schematics of facets formation during directional solidification (a, b) at sample boundaries and (c, d) at a grain boundary. Note that distinction between μ cells at edges and in the bulk of the CA grid is simply made by considering neighborhood. With the chosen Moore configuration, a bulk cell has $N = 8$ neighbors ($N = 26$ in 3D) while an edge cell necessarily has less than N neighbors. The selected {11} facets ({111} in 3D) are deduced from geometrical considerations.

In the case of a grain in connection with an edge (a, b), a local frame V_g is defined. It is centered in $G(x_\mu + l_{CA}/2,\ y_\mu - l_{CA}/2)$ with perpendicular ⟨10⟩ directions (⟨100⟩ in 3D) for unit vectors. Coordinates of the liquid cell μ in frame V_g are then computed, $(\tilde{x}_\mu, \tilde{y}_\mu)_g$ ($(\tilde{x}_\mu, \tilde{y}_\mu, \tilde{z}_\mu)_g$ in 3D), the sign of which are used to define the normal of the facet, $\boldsymbol{n}^{\{11\}}$ ($\boldsymbol{n}^{\{111\}}$ in 3D). Applied to the vertical left-hand-side (LHS) sample edge in Fig. 5(b) by considering the liquid cell μ_1 at the time of capture with the corresponding frame V_g centered in G_1 defined by cell μ_1, coordinates are $\tilde{x}_{\mu_1} < 0$ and $\tilde{y}_{\mu_1} > 0$ leading to selection of the $(\bar{1}1)$ facet with $a_g^{(\bar{1}1)} = -1$ and $b_g^{(\bar{1}1)} = 1$. The $(\bar{1}1)$ plane is activated if $\Delta T_{\mu_1} < \Delta T_g^{(\bar{1}1)}$. Similarly at the vertical right-hand-side (RHS) sample edge in Fig. 5(b) by considering the liquid cell μ_2 at the time of capture with the corresponding frame V_g centered in G_2 defined by cell μ_2, coordinates are $\tilde{x}_{\mu_2} > 0$ and $\tilde{y}_{\mu_2} > 0$ leading to selection of the (11) facet with $a_g^{(11)} = 1$ and $b_g^{(11)} = 1$. The (11) plane is activated if $\Delta T_{\mu_2} < \Delta T_g^{(11)}$. Upon activation, an initial value is computed for coefficients $c_g^{\{11\}}$ using $c_{g,t_0}^{\{11\}} = -\left(a_g^{\{11\}} x_\mu + b_g^{\{11\}} y_\mu\right)$ where t_0 is the time at {11} facet activation of grain g, i.e. $c_{g,t_0}^{(\bar{1}1)}$ and $c_{g,t_0}^{(11)}$ if both facets are activated in Fig. 5(b). The Cartesian equation of all activated facets is then fully determined. The corresponding procedure is applied in 3D.

A similar approach is applied to identify the most favorable planes that will potentially lead to the formation of faceted grooves at grain boundaries. A bulk liquid cell μ being captured is tested for being at a grain boundary. This is done by seeking for at least two different grain indexes among its neighboring captured cells. The {11} plane identification ({111} in 3D) for each grain found (g_1 and g_2 in Fig. 5 (c)) is achieved by using coordinates of cell center C_μ and frames V_g associated to each grain (V_{g_1} and V_{g_2} in Fig. 5(c)) defined by the same coordinates center G positioned between cells in the closest grid direction opposite to the temperature gradient ($(x_\mu,\ y_\mu - l_{CA}/2)$ in Fig. 5(d)). The unit vectors of the frames V_g correspond to perpendicular ⟨10⟩ directions (⟨100⟩ in 3D) of grains g (g_1 and g_2 defined by ϕ_1 and ϕ_2 in Fig. 5(c), respectively). They are deduced from coordinates of cell μ in frame V_g, $(\tilde{x}_\mu, \tilde{y}_\mu)_g$ ($(\tilde{x}_\mu, \tilde{y}_\mu, \tilde{z}_\mu)_g$ in 3D), the sign of which are used to define the normal of the selected facet $\boldsymbol{n}^{\{11\}}$ ($\boldsymbol{n}^{\{111\}}$ in 3D). Applied to the configuration in Fig. 5(c) by considering liquid cell μ at the time of capture with frame V_{g_1}, coordinates are $(\tilde{x}_\mu > 0,\ \tilde{y}_\mu > 0)_{g_1}$ leading to selection of the (11) facet with $a_{g_1}^{(11)} = 1$ and $b_{g_1}^{(11)} = 1$

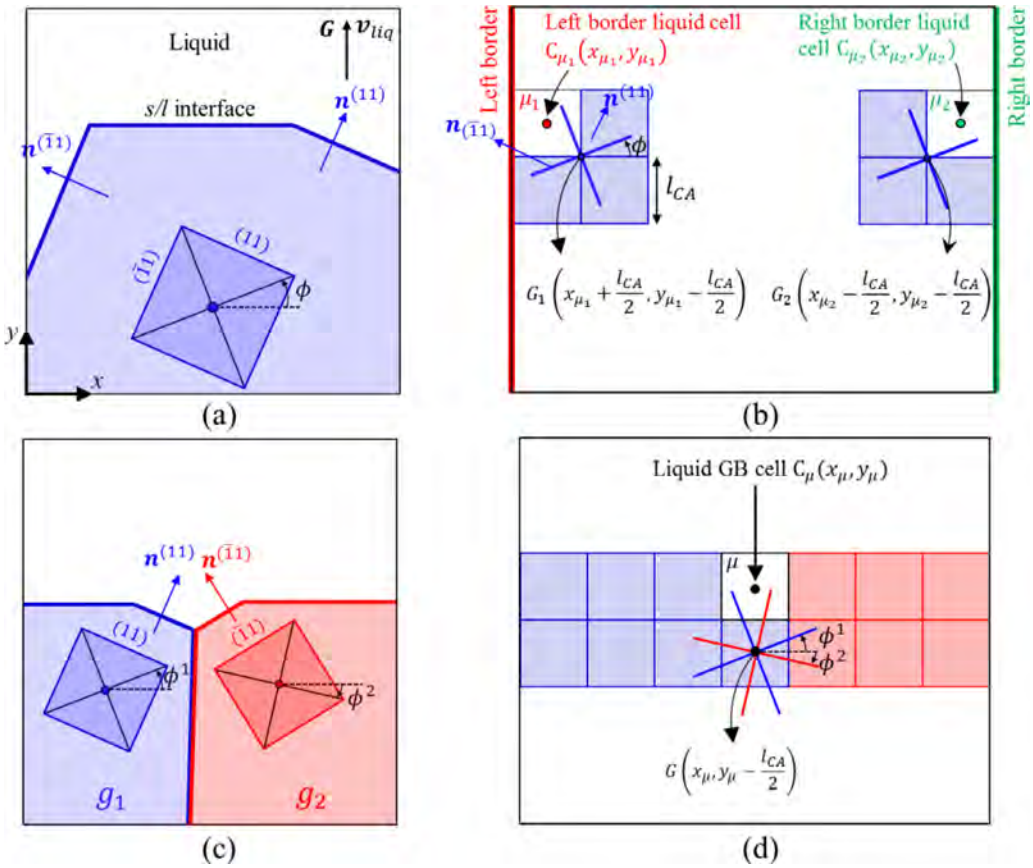

Fig. 5. Identification of {11} planes for faceted growth during directional solidification are sketched in 2D for (a, b) a grain in contact with vertical sample edges and (c, d) two grains forming a grain boundary with no Σ3 relationship. Liquid cells (b) μ_1 and μ_2 being captured by the solidification front are represented, together with two frames V_g defined by the perpendicular ⟨10⟩ directions of the grain g and centered in G_1 and G_2. In case of a (d) grain boundary, frames V_{g_1} and V_{g_2} defined by the perpendicular ⟨10⟩ directions of grains g_1 and g_2 are shown, both centered in G.

and $(\tilde{x}_\mu < 0, \tilde{y}_\mu > 0)_{g_2}$ leading to selection of the $(\bar{1}1)$ facet with $a_{g_2}^{(\bar{1}1)} = -1$ and $b_{g_2}^{(\bar{1}1)} = 1$. Consequently, the selected planes for growth at the grain boundary are the (11) plane from g_1 and the $(\bar{1}1)$ plane from g_2.

Again, activation of facets will take place on g_1 if $\Delta T_\mu < \Delta T_{g_1}^{(11)}$, on g_2 if $\Delta T_\mu < \Delta T_{g_2}^{(\bar{1}1)}$, or simultaneously on both grains if the latter two conditions are fulfilled. Upon activation, an initial value is computed for coefficient $c_g^{\{11\}}$ using $c_{g,t_0}^{\{11\}} = -(a_g^{\{11\}} x_\mu + b_g^{\{11\}} y_\mu)$, where t_0 is the time at {11} facet activation of grain g. A similar procedure is applied in 3D.

3.3.2. Facet growth

Facets of a grain g being described by its Cartesian equation $D_g^{\{11\}}: a_g^{\{11\}} x + b_g^{\{11\}} y + c_g^{\{11\}} = 0$ ($D_g^{\{111\}}: a_g^{\{111\}} x + b_g^{\{111\}} y + c_g^{\{111\}} z + d_g^{\{111\}} = 0$ in 3D), its growth is simply modeled by the time integration of the crystal growth velocity of the {11} facets $\boldsymbol{v}_c^{\{11\}}$ ($\boldsymbol{v}_c^{\{111\}}$ in 3D) defined along the normal $\boldsymbol{n}^{\{11\}}$ ($\boldsymbol{n}^{\{111\}}$ in 3D). In practice it is sufficient to update with time coefficient $c_g^{\{11\}}$ ($d_g^{\{111\}}$ in 3D) using:

$$c_g^{\{11\}} = v_c^{\{11\}}(t - t_0) + c_{g,t_0}^{\{11\}} \left(d_g^{\{111\}} = v_c^{\{111\}}(t - t_0) + d_{g,t_0}^{\{111\}} \text{ in 3D}\right). \quad (2)$$

The algorithm described above (Fig. 4) is modified. This is achieved by conditioning the capture of a liquid cell μ by the growing cell ν belonging to grain g considering its location with respect to the facets described by their Cartesian equations. The cell center C_μ of coordinates (x_μ, y_μ) ((x_μ, y_μ, z_μ) in 3D) is injected in the equation of the activated facets of grain g to compute the quantity $a_g^{\{11\}} x_\mu + b_g^{\{11\}} y_\mu + c_{g,t_0}^{\{11\}}$ ($a_g^{\{111\}} x_\mu + b_g^{\{111\}} y_\mu + c_g^{\{111\}} z_\mu + d_{g,t_0}^{\{111\}}$ in 3D). The capture is implemented if a negative value is gained, it is otherwise inhibited. This condition corresponds to the facet overpassing the cell center. In case of capture, the same rules as for the standard growth algorithm are applied to update cell indexes. Figure 6 gives an illustration. In Fig. 6(a), despite the fact that the growth envelope of cell ν encompasses the neighboring liquid cell μ_N and μ_W, capture cannot proceed as the already activated (11) facet has not overpassed cell centers C_{μ_N} and C_{μ_W} at time t. One has to wait until $t + \Delta t$ sketched in Fig. 6(b), so that the facet position using Eq. (2) is updated and has overpassed the cell center μ_W that is now captured. Cell μ_N is captured only after further growth of the (11) facet. The capture algorithm is thus referred to as a *conditioned* capture algorithm. Additionally, the parameter $v_c^{\{11\}}$ ($v_c^{\{111\}}$ in 3D) is a user-defined parameter of the model.

3.3.3. Rough to faceted growth transition

A preliminary 2D illustration is given in Figure 7. It considers the growth of a single grain nucleated in a 0.02 m × 0.02 m square cavity. The aim is to provide the reader with a better understanding of the conditioned capture algorithm and its associated effects by comparing its results with the standard algorithm. The linear expression of velocity and the corresponding value of $A = 8 \cdot 10^{-6}$ m s^{-1} K^{-1} are deduced from experimental observations of pure silicon growth available in the literature [45]. The simulation domain is fully covered by a CA grid of constant cell size, $l_{CA} = 20 \cdot 10^{-6}$ m. The origin, O, of the reference frame is located at the bottom-left corner of the domain. The temperature field is imposed onto the whole domain and cooling is applied using the frozen temperature gradient approximation [44]. The temperature evolution at any point P is expressed as:

$$T(y_P, t) = T_0 + G\, y_P + \dot{T}\, t \quad (3)$$

where G is a constant temperature gradient, $\dot{T}$ a constant cooling rate and $T_0 = T(O,\ t = 0 \text{ s})$ is the temperature at the origin of the domain at the start of the simulation. The grain nucleates at the center of the domain with crystallographic orientation $\phi = 0°$. Fig. 7(a) and (b) first show the simulation results corresponding to $G = 0$ K m^{-1} and $\dot{T} = 0$ K s^{-1}. Consequently, a stationary and uniform temperature field is imposed at $T = T_0 = 1685$ K. With melting temperature of silicon at $T_M = 1687$ K, the corresponding undercooling is $\Delta T = 2$ K. According to Eq. (1), these parameters lead to a constant growth velocity in the ⟨10⟩ directions $v^{\langle 10\rangle} = 16$ μm s^{-1} and to a growth velocity in the ⟨11⟩ directions $v^{\langle 11\rangle} = v^{\langle 10\rangle}/\sqrt{2} = 11.3$ μm s^{-1}. All {11} planes of the grain thus grow at a constant velocity $v^{\{11\}} = 11.3$ μm s^{-1}. The normal distribution law for the activation undercooling of the {11} facets is given by $\Delta T_{g,m}^{\{11\}} = 3$ K and $\Delta T_{g,s}^{\{11\}} = 0$ K. These values are chosen for illustration purpose so that all facets are activated with $\Delta T_g^{\{11\}} = 3$ K. Since the grain nucleates at an undercooling $\Delta T = 2$ K, all liquid cells are captured with an undercooling lower than the activation undercooling of the {11} virtual planes, the later thus being activated at the first time step of the simulation. Fig. 7(a) compares the result of the computed grain envelope growth using the standard capture algorithm (in blue) and the conditioned capture algorithm (in red) defined by a constant {11} plane growth velocity, $v_c^{\{11\}} = 10$ μm s^{-1}, i.e. lower than the one given by the growth kinetic law. The time step is fixed at $\Delta t = 1$ s and the growth envelopes are drawn at time $t \in \{100, 200, 300, 400, 500\}$ s. With the standard capture algorithm and the constant velocity for the ⟨10⟩ (and consequently, ⟨11⟩)

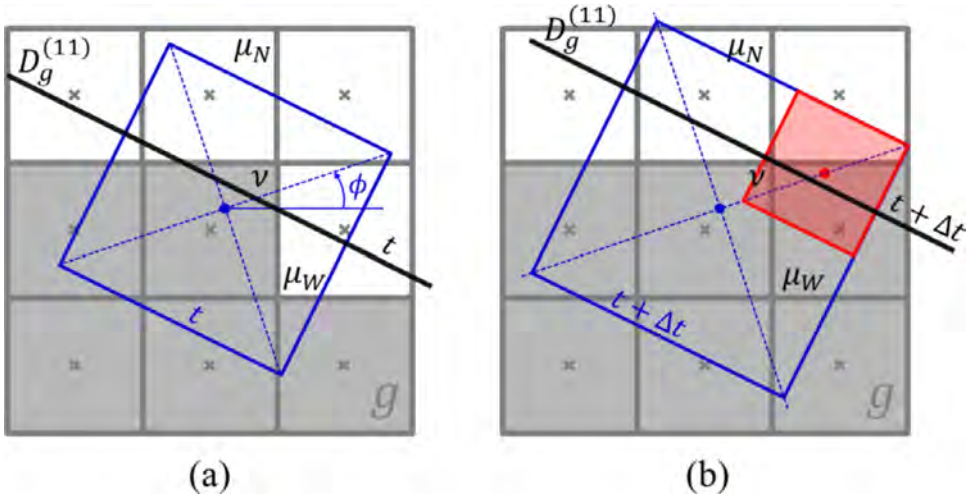

Fig. 6. Schematics of the *conditioned* capture algorithm due to the growth of an active (11) facet of grain g showing (a) the envelope at time t associated to a given solid cell ν and the position of the $D_g^{(11)}$ growing plane. Envelope of cell ν has overlapped both the centers of liquid cell μ_N (North) and μ_W (West). However, those cells remain in a liquid state since their centers were not overpassed by $D_g^{(11)}$ at time t. This is achieved at a later time only for cell μ_W as shown in (b). The capture of cells μ_W is thus made while cell μ_N is captured after further growth of the (11) facet.

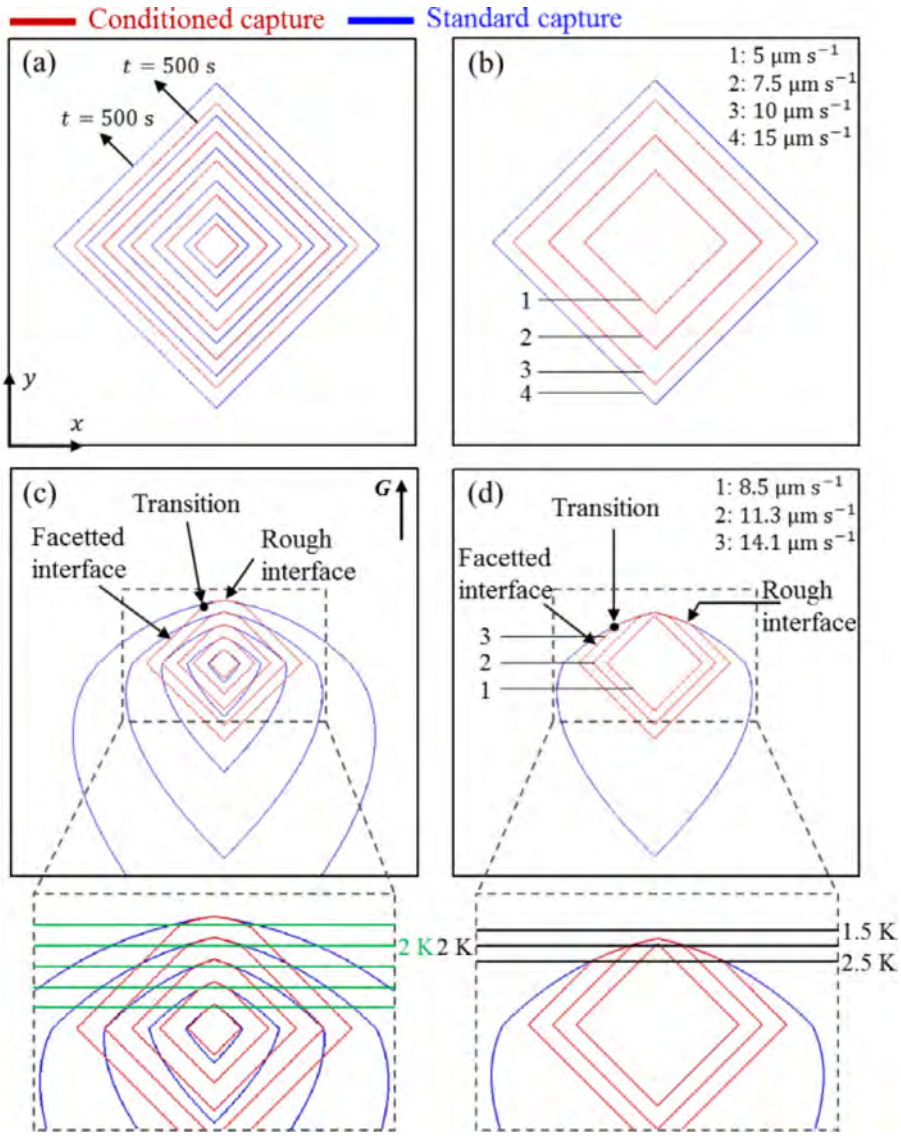

Fig. 7. Simulated growth of the grain envelope for an equiaxed grain nucleated at the center of a square domain using (blue) the standard capture algorithm and (red) the conditioned capture algorithm. Parameters are (a, b) uniform and constant temperature with $v^{\langle 10\rangle} = 16\ \mu\text{m s}^{-1}$, (a) $v_c^{\{11\}} = 10\ \mu\text{m s}^{-1}$ with grain envelopes drawn at times $t \in \{100, 200, 300, 400, 500\}$ s and (b) $v_c^{\{11\}} \in \{5,\ 7.5,\ 10,\ 15\}\ \mu\text{m s}^{-1}$ with grain envelopes drawn at time $t = 500$ s; (c, d) non-uniform temperature field ($G = 1200\ \text{K}\cdot\text{m}^{-1}$, $\dot{T} = -0.016\ \text{K}\cdot\text{s}^{-1}$), (c) $v_c^{\{11\}} = 11.3\ \mu\text{m s}^{-1}$ with grain envelopes drawn at times $t \in \{40, 80, 120, 160, 200\}$ s and (b) $v_c^{\{11\}} \in \{8.5,\ 11.3,\ 14.1\}\ \mu\text{m s}^{-1}$ with grain envelopes drawn at time $t = 200$ s. The isotherms where transition takes place from rough to faceted grain envelopes are drawn (c) at the selected times and correspond to a fixed undercooling equal to 2 K and (d) for the various $v_c^{\{11\}}$ values.

directions, the blue grain envelope squares are regularly spaced with time. The same observation is made for the conditioned capture algorithm but with a lower velocity of the virtual planes ($v_c^{\{11\}} < v^{\langle 11\rangle}$), a smaller distance between each red successive envelope is found. In other words, for a given liquid cell, its capture will always be delayed compared to the standard growth algorithm. Fig. 7(b) shows the effect of progressively increasing the $v_c^{\{11\}}$ velocity from 5 μm s^{-1} to 15 μm s^{-1} by comparing the grain envelope shape at a given time, $t = 500$ s, with the largest blue and red envelopes drawn in Fig. 7(a). As can be seen, the grain growth is constrained by the virtual {11} planes for $v_c^{\{11\}} < v^{\{11\}}$ so the red envelopes for $v_c^{\{11\}} = 5\ \mu\text{m s}^{-1}$ and $v_c^{\{11\}} = 7.5\ \mu\text{m s}^{-1}$ are smaller than for $v_c^{\{11\}} = 10\ \mu\text{m s}^{-1}$. However, for $v_c^{\{11\}} = 15\ \mu\text{m s}^{-1}$, i.e. $v_c^{\{11\}} > v^{\{11\}}$, the grain envelope is the same as for the standard algorithm so the blue and red envelopes are superimposed. The maximum propagation of the grain envelope is thus given by the standard algorithm. The reason is that capture due to the propagation of the virtual facets cannot operate beyond the first nearest neighboring liquid cells. In other words, the virtual plane has propagated beyond this limit and is not reachable anymore by the growth front. So, for large value of $v_c^{\{11\}}$, one could say that the grain envelope is the result of the standard capture algorithm.

In order to model a rough to faceted interface transition, we now consider a non-uniform temperature field, i.e. $G \neq 0$ K m^{-1}. Fig. 7(c) and (d) show external grain envelopes using both the standard and the conditioned capture algorithms at times $t \in \{40, 80, 120, 160, 200\}$ s and for a given time with different $v_c^{\{11\}}$, respectively. Both the temperature gradient G and the cooling rate $\dot{T}$ are constant: $G = 1200$ K m^{-1} and $\dot{T} = -0.016$ K s^{-1}. The initial temperature T_0 at the origin, O, of the domain is set to 1673 K in order to have, as in the previous case, an initial undercooling $\Delta T = 2$ K at the center of the domain where the grain nucleates. In Fig. 7(c) the conditioned capture algorithm is applied with $v_c^{\{11\}} = 11.3\ \mu\text{m s}^{-1}$, i.e. a corresponding virtual growth kinetic in the $\langle 10\rangle$ directions equal to $\sqrt{2}\ v_c^{\{11\}} = 16\ \mu\text{m s}^{-1}$ and an equivalent undercooling $\Delta T = 2$ K for the $\langle 10\rangle$ directions with Eq. (1). The standard capture algorithm implies that the growth kinetics of cell envelopes depends on the local undercooling ΔT in a non-uniform temperature field. Thus, cells

enduring growth undercooling ΔT higher than 2 K have a growth kinetic $v^{\{11\}}$ higher than $v_c^{\{11\}}$ leading to an external envelope being constrained by the {11} virtual planes. This explains why all red boundaries in Fig. 7 (c) are within the corresponding blue envelopes defined at a given time. For the top regions of the s/l boundaries where $v^{\{11\}} < v_c^{\{11\}}$, the red and blue grain boundaries are superimposed as the virtual planes are out of reach for capture by neighboring cells. The condition $v^{\{11\}} = v_c^{\{11\}}$ thus defines the rough to faceted interface transition when using the conditioned capture algorithm. In the magnified region located below Fig. 7 (c), horizontal green lines are added. They represent isotherms $\Delta T = 2$ K at the displayed times. At this undercooling, as stated above, $v^{\{11\}} = v_c^{\{11\}}$. At a given time, the bottom part of the red grain envelope, located below the isotherm in a colder region with higher undercooling, is faceted as $v^{\{11\}} > v_c^{\{11\}}$. Oppositely, the upper part of the grain envelope, located above the isotherm with lower undercooling, is rough and coincide with the result of the standard growth algorithm. Fig. 7(d) shows the external grain envelope at the instant $t = 200$ s resulting from both the standard and the conditioned capture algorithms with values of $v_c^{\{11\}} = 8.5$ μm s^{-1}, 11.3 μm s^{-1} and 14.1 μm s^{-1} corresponding to undercoolings $\Delta T = 1.5$ K, 2 K and 2.5 K, respectively (represented by horizontal black lines in the magnified region). Similarly, at undercoolings of the local growth envelope larger than 1.5 K, 2 K and 2.5 K, faceted growth is obtained.

3.4. Twin relationship and growth

3.4.1. Twin relationship

Nucleation undercooling of grains in twin relationships on {111} facets are defined at sample edge, $\Delta T_{N,T}^{E}$, and at grain boundary groove, $\Delta T_{N,T}^{B}$ (i.e. in the bulk material). This is to cope with experimental observations showing that twin formation upon directional solidification is only of $\Sigma 3$ type and $\Delta T_{N,T}^{B} < \Delta T_{N,T}^{E}$ [3,42]. Upon capture of a liquid cell μ by its neighboring growing cell ν, location of cell μ is tested to determine if it is located on a sample edge or as part of the bulk. For an edge cell (respectively a bulk cell), if the test $\Delta T_\mu > \Delta T_{N,T}^{E}$ (respectively $\Delta T_\mu > \Delta T_{N,T}^{B}$), is verified, a nucleation event takes place. The Euler angles of the new grain formed in cell μ must correspond to the crystallographic orientations of the capturing grain to which a $\Sigma 3$ twin rotation around the normal to the capturing facet is applied. It is worth noticing that no other twin relationship is considered for nucleation events as experimental observations report that $\Sigma 9$, $\Sigma 27$ or higher order twin relationships in directionally solidified silicon are only the results of growth competition of grains formed in $\Sigma 3$ relationship [3,42]. If a liquid cell μ is located at the boundary between two grains g_1 and g_2, the usual growth conditions are considered. In most cases only one of the neighboring growing cells belonging to grains g_1 and g_2 is able to capture the liquid cell μ. However, the liquid cell μ can occasionally be geometrically captured during the same time increment by the envelopes associated to cells belonging to grains g_1 and g_2. In such condition, the largest capturing envelope associated to the growing cells is considered, hence selecting the grain defining twinning. A single capture event is consequently always applied to a liquid cell. Note that this situation only occurs when the time step is not sufficiently small.

Both $\Delta T_{N,T}^{E}$ and $\Delta T_{N,T}^{B}$ are constant parameters for nucleation of grains in twin relationships on {111} facets. The activation undercooling of the {111} facets is given by a Gaussian distribution. This is sufficient to generate irregular bands of twinned grains. It is also worth mentioning that the algorithm only permits the growth of one grain in twin relationship for each {111} facet.

The CA capture algorithm has to be modified since the crystallographic orientation of the grain in cell μ is not identical to the one in cell ν. A $\Sigma 3$ twin relationship corresponds to a 60° rotation around the normal to the {111} capturing facet. This step is sketched in Figure 8 considering a nucleation event at the edge of the sample. As 2D approximation cannot reproduce well this operation, the crystallographic orientation ϕ^T of the growth envelope associated to the grain in twin relationship located in cell μ is arbitrarily chosen. In 3D, Euler angles of a newly created grain in twin relationship are denoted $(\phi_1^T, \phi^T, \phi_2^T)$. Their values are deduced as a function of the original orientation of the grain in the capturing cell ν, (ϕ_1, ϕ, ϕ_2), and the rotation matrix M expressing the relative orientation of the crystal directions ⟨100⟩ into the reference frame of the sample:

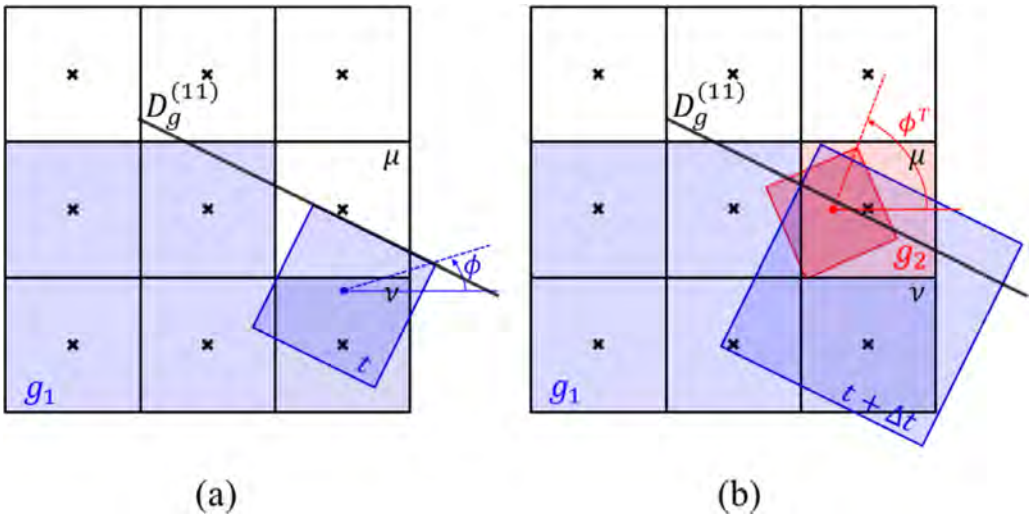

Fig. 8. Schematic representation of (a) the growth of grain $g = \phi$ from cell ν with the conditioned capture algorithm and (b) the nucleation a grain $g^T = \phi^T$ in twin relationship with g in cell μ at a sample edge due to an undercooling ΔT_μ larger than the nucleation undercooling $\Delta T_{N,T}^{E}$. A new growth envelope is associated to cell μ with crystallographic orientation ϕ^T corresponding to a $\Sigma 3$ twin rotation (arbitrary rotation in 2D). In 3D, $g^T = (\phi_1^T, \phi^T, \phi_2^T)$ is computed using Eq. (6) from $g = (\phi_1, \phi, \phi_2)$.

$$M = \begin{pmatrix} \cos\phi_1\cos\phi_2 - \cos\phi\sin\phi_1\sin\phi_2 & -\cos\phi\cos\phi_2\sin\phi_1 - \cos\phi_1\sin\phi_2 & \sin\phi\sin\phi_1 \\ \cos\phi_2\sin\phi_1 + \cos\phi\sin\phi_1\sin\phi_2 & \cos\phi\cos\phi_1\cos\phi_2 - \sin\phi_1\sin\phi_2 & -\cos\phi_1\sin\phi \\ \sin\phi\sin\phi_2 & \cos\phi_2\sin\phi & \cos\phi \end{pmatrix}. \tag{4}$$

The matrix corresponding to a rotation of angle θ around a unitary vector $\boldsymbol{u}(u_x, u_y, u_z)$ is given by:

$$R = \begin{pmatrix} u_x^2(1-c)+c & u_xu_y(1-c)-u_zs & u_xu_z(1-c)+u_ys \\ u_xu_y(1-c)+u_zs & u_y^2(1-c)+c & u_yu_z(1-c)-u_xs \\ u_xu_z(1-c)-u_ys & u_yu_z(1-c)+u_xs & u_z^2(1-c)+c \end{pmatrix} \tag{5}$$

where $c = \cos\theta$ and $s = \sin\theta$. With $\theta = 60^\circ$ and $\boldsymbol{u} = \boldsymbol{n}^{\{111\}}$ the normal vector to the {111} twin plane, $R = R_{\Sigma 3}$. The rotation matrix transforming the twin grain frame into the sample frame of reference is $M^T = M \cdot R_{\Sigma 3}$. So, writing the rotation matrix M^T for grain g^T, (ϕ_1^T, ϕ^T, ϕ_2^T), using Eq. (4) and identifying each term with the product $M \cdot R_{\Sigma 3}$ yields the following result:

$$\begin{cases} \phi_1^T = atan2(M_{13}^T, -M_{23}^T) \\ \phi^T = \cos^{-1}(M_{33}^T) \\ \phi_2^T = atan2(M_{31}^T, M_{32}^T) \end{cases}. \tag{6}$$

3.4.2. Growth in twin relationship

Twin boundaries between grains are locked during growth [3,42]. To maintain the twin boundary while pursuing growth of the s/l interfaces, the conditioned capture algorithm is used. Yet, the twin grain boundary remains static in space and develops as a result of growth of the grains on each side of the corresponding {111} facet. Note that this is equivalent to keep a constant value for $d_{g,t_{N,T}}^{\{111\}}$ in Eq. (2), defined at the time $t_{N,T}$ of the nucleation of the grain in twin relationship. The capture algorithm is modified as schematized in Figure 9. Grains g_1 and g_2 develop in twin relationship and the fixed twin plane $D_{g_1}^{(11)}$ is displayed at time t in Fig. 9(a). At a later time $t + \Delta t$ shown in Fig. 9(b), the position of the twin plane $D_{g_1}^{(11)}$ is unchanged but the liquid cell μ_1 could be captured by grain g_1 and g_2 according to the displayed growing shapes. However, because it is located above $D_{g_1}^{(11)}$, only the capture by g_2 is authorized, capture by grain g_1 being inhibited. Similarly, capture of cell μ_2 is only possible by grain g_1 localized beneath $D_{g_1}^{(11)}$. This procedure is used as long as the two grains in $\Sigma 3$ twin relationship are in contact. If grain g_1 stops, i.e. does not grow anymore as it is fully surrounded by non-liquid cells, the conditioned capture is no longer applied to g_2.

4. Results and discussions

The 3D CA model described above is applied to simulate experimental observations obtained by X-ray imaging reported in details elsewhere [3,4,40,42]. Properties and parameters T_M, A, $v_c^{\{111\}}$, $\Delta T_{N,T}^E$, $\Delta T_{N,T}^B$, (ϕ_1, ϕ, ϕ_2), G and $\dot{T}$ listed in Table 1 are taken from the experimental data. Simulations are performed in a rectangular domain of height H, width W and thickness E, corresponding to lengths along the x-, y- and z- directions, respectively. The bottom-left corner of the domain defines the origin point O with coordinates $(x_O, y_O, z_O) = (0, 0, 0)$. Consequently, all points in the domain have positive coordinates (x, y, z) with $0 \le x \le H, 0 \le y \le W$ and $0 \le z \le T$. The temperature field is imposed onto the whole domain. In order to reflect the experimental configuration, a frozen temperature gradient is imposed, slightly misaligned with the vertical x-axis by a $\beta = -5^\circ$ rotation about the z-axis [45], leading to isothermal surfaces slightly off yz-planes. The temperature evolution at position (x, y, z) and time t is then computed using the following analytical expression:

$$T(x,\ y,\ z,\ t) = T_0 + G\cos\beta\ x + G\sin\beta\ y + \dot{T}\ t \tag{7}$$

where $T_0 = T(O,\ t = 0\ s)$ is the temperature at the origin of the domain at the beginning of the simulation. One should note that this approximation is not common in previous work with the CA-FE model where full coupling is achieved between the development of the grain structure and the heat flow [22,23,25–29]. However, in the present experimental configuration, the temperature field is well controlled and characterized, only leading to constrained growth [46]. The solution of the energy balance then becomes optional, i.e. the temperature gradient around the solidification front is little modified by the release of latent heat. Consequently, a known temperature field can be imposed. The time increment, Δt, between two temperature computed fields with Eq. (7), is chosen to ensure that the growth front propagates on a distance smaller than the cell size, l_{CA}, by considering the ratio $l_{CA}/v_L = -l_{CA}G/\dot{T}$.

4.1. Grain boundary grooves

Simulations are first performed by fully covering the bottom of the domain with 2 seeds. The seeds represent 2 grains of different orientations separated by the $y = W/2$ plane but limited to a single row of grid cells located at the bottom of the domain in the yz-plane with minimum x-coordinate. This is simply achieved by adequately

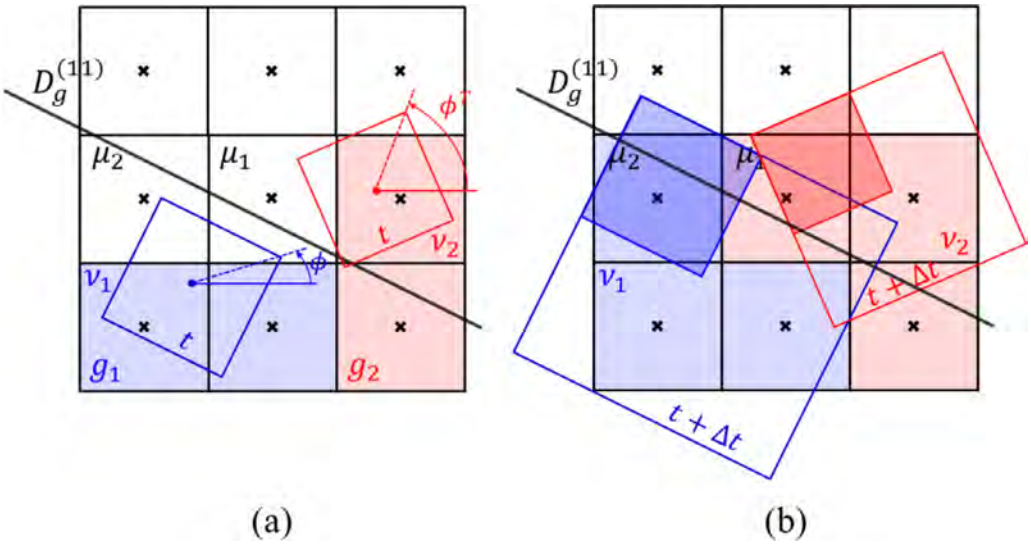

Fig. 9. Schematics of the twin growth algorithm showing (a) at time t the growth envelopes associated to cells ν_1 and ν_2 belonging to grains g_1 and g_2 located on each side of a {11} twin boundary plane $D^{(11)}$ and (b) at a later time $t + \Delta t$ the capture of two liquid cells μ_1 and μ_2 taking into account their spatial position with respect to $D^{(11)}$ together with their initial growth shape.

Table 1
Properties of pure silicon, process parameters and simulation parameters.

	Symbol	Value			Unit
		Figure 1(a), 10	Figure 1(b), 11	Figures 2, 12-15	
Material properties					
Melting temperature	T_M	1687	1687	1687	K
Linear growth law parameters	A	$8 \cdot 10^{-6}$	$8 \cdot 10^{-6}$	$8 \cdot 10^{-6}$	m s^{-1} K^{-1}
{111} facet growth velocity	$v_c^{\{111\}}$	$8 \cdot 10^{-6}$	$8 \cdot 10^{-6}$	$8 \cdot 10^{-6}$	m s^{-1}
Nucleation undercooling (edge)	$\Delta T_{N,T}^{E}$	–	–	2.1	K
Nucleation undercooling (groove)	$\Delta T_{N,T}^{B}$	–	–	*1.8*	K
Grains orientation (initial seed)	(ϕ_1, ϕ, ϕ_2)	(g_1) (223.8, 28.3, 15.3) (g_2) (95.1, 48.3, 62.1)	(g_1) (17.6, 88.3, −43.4) (g_2) (–21.3, 89.7, 47.3)	(356, 44, 3)	(°, °, °)
Process parameters					
Initial temperature	T_0	1686	1686	1686	K
Measured temperature gradient	G	2200	1200	*1200*	K m^{-1}
Cooling rate	$\dot{T}$	–0.003	–0.016	–0.016	K s^{-1}
Simulation parameters					
Cell size	l_{CA}	$25 \cdot 10^{-6}$	$25 \cdot 10^{-6}$	$25 \cdot 10^{-6}$	m
Domain thickness	E	$300 \cdot 10^{-6}$	$300 \cdot 10^{-6}$	$300 \cdot 10^{-6}$	m
Domain width	W	$4 \cdot 10^{-3}$	$4 \cdot 10^{-3}$	$4 \cdot 10^{-3}$	m
Domain length	H	$7.2 \cdot 10^{-3}$	$7.2 \cdot 10^{-3}$	$7.2 \cdot 10^{-3}$	m
Time step	Δt	1	1	1	s
Mean activation undercooling	$\Delta T_{g,m}^{\{111\}}$	(g_1) 2, (g_2)–	2	2	K
Standard deviation undercooling	$\Delta T_{g,s}^{\{111\}}$	0	0	0.1	K

initializing the cell and grain index of these cells. The grain orientations are reported in Fig. 1 and in Table 1. The first experimental situation shown in Fig. 1(a) is duplicated in Figure 10(a) for comparison with simulation results given in Fig. 10(b) and 10(c). The same is done with Fig. 1(b) and Figure 11.

In Fig. 10, only the LHS red grain g_1 develops a {111} facet. It is identified as the $(11\bar{1})$ facet. For that purpose, the activation undercooling of the {111} facets of grain g_1 was taken equal to $\Delta T_{g_1,m}^{\{111\}} = 2$ K. This is achieved by fixing a zero value for the standard distribution, $\Delta T_{g_1,s}^{\{111\}} = 0$ K. None of the {111} facets of the RHS blue grain g_2 was activated. The reason is that their activation undercooling was set negative, $\Delta T_{g_2}^{\{111\}} < 0$ K, so that the condition for activation was never met. Note that nucleation of a grain in twin relationship with the $(11\bar{1})$ facet of grain g_1 was also inhibited by choosing a very large value of the nucleation undercooling. A resulting grain boundary groove of type faceted/rough is formed by the interaction of the $(11\bar{1})$ facet of grain g_1 and the rough interface of grain g_2. It is worth noting that simulation retrieves the shape of the groove observed in Fig. 10(a) but also the orientation of the grain boundary that follows the $(11\bar{1})$ facet of grain g_1. This is in agreement with previous theoretical model [19]. The orientation of the grain boundary is very close to the experimental measurement and is maintained upon growth as shown by comparing Fig. 10(b) and Fig. 10(c). Also note that the rounded shape of the solid-liquid interface for grain g_2 is the result of a stationary situation similar to that already described analytically by de Bussac and Gandin where a rough grain interface with anisotropic growth kinetics defined along <100> directions interact with a locked boundary [47]. Such result was thus anticipated.

Fig. 11 shows the situation where a faceted/faceted groove forms. This is the result of the identification, activation and growth in interaction of two facets. The same values are used for the distribution of activation undercooling of the facets of the 2 grains by fixing equal mean value and a zero standard deviation. Only one facet forms on each grain at the grain boundary as a result of the rough-to-faceted transition. The facets being more undercooled than the rough s/l interface, they are found in contact at the grain boundary and permit the development of the groove. As in the previous case, nucleation of grains in twin relationship is inhibited. In the constant z cut, the simulated angle made by the two competing {111} facets forming the grain boundary groove is close to measurement. Upon stationary growth, the orientation of the grain boundary remains unchanged as shown by Fig. 11(b) and (c).

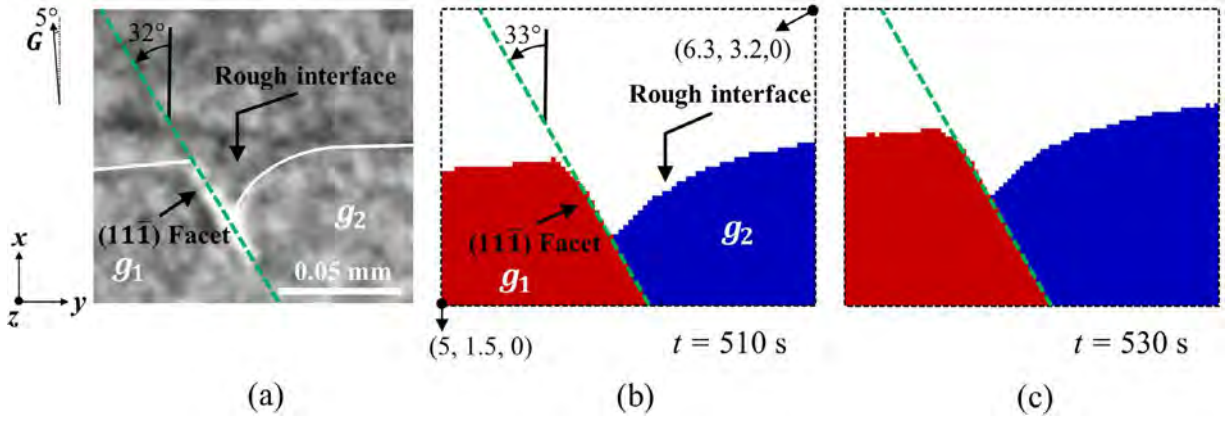

Fig. 10. Growth of a faceted/rough boundary groove in silicon (a) as observed by X-ray radiography during directional solidification and (b, c) as computed by the 3D CA model at time (b) 510 s and (c) 530 s. The orientation of the grain boundary is measured by the green dashed line. It is close to the measurement and defined by the activated {111} facet as proposed theoretically [19] and observed experimentally [40,42]. Coordinates of the bottom-left and top-right corners are given in *mm*. See Table 1 for simulation parameters.

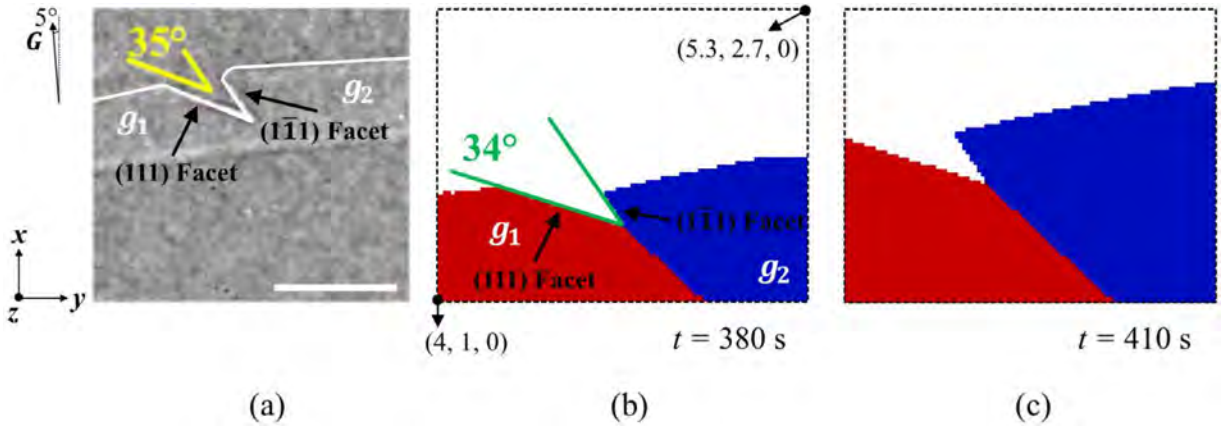

Fig. 11. Growth of a faceted/faceted boundary groove in silicon (a) as observed by X-ray radiography during directional solidification and (b, c) as computed by the 3D CA model at time (b) 380 s and (c) 410 s. The simulated angle formed between the two facets, 34°, compares favorably with the measurement, 35°. Coordinates of the bottom-left and top-right corners are given in *mm*. See Table 1 for simulation parameters.

4.2. Twinning sequence

The next result concerns the growth of a unique seed covering the whole bottom surface of the domain with values coming from measurements of the experiment reported in Figs. 2 and 3 [4,40]. The normal distribution law of undercooling to activate the {111} facets has to be carefully defined considering *i*- the stationary undercooling associated to the isotherm velocity, $\Delta T = v_L/A = -\dot{T}/(GA)$ and *ii*- the undercooling for the twin nucleation events, different at edges and in the bulk [42]. Note that the latter quantities are estimated from measurements so that only the activation undercooling of the facets remains as a parameter. In the simulation shown in Figure 12, nucleation of new grains in twin relationship always occurs at a nucleation undercooling $\Delta T^{E}_{N,T} = 2.1$ K on edges. After a nucleation event, if the new grain does not develop a {111} facet, the local undercooling at the bottom of the facet decreases from nucleation undercooling $\Delta T^{E}_{N,T}$ to stationary undercooling $\Delta T = 1.67$ K. In order to possibly activate and grow the common {111} facet, activation undercooling thus has to be higher than 1.67 K. Similarly, if the activation undercooling is higher than the nucleation undercooling, i.e. 2.1 K, the new twin grain grows a {111} facet right after its nucleation, thus leading to a very narrow twin band. Consequently, mean activation, $\Delta T^{\{111\}}_{g,m}$, and standard deviation, $\Delta T^{\{111\}}_{g,s}$, undercoolings are chosen respectively equal to 2.0 K and 0.1 K. Grains in twin relationship thus have high probability to activate and grow a new {111} facet during growth which is consistent with the experimental observations. Smooth simulations for the sequence of activation and growth of the facets also require a good definition of the temperature field among the cells. This is achieved by choosing a cell size smaller than the typical distance corresponding to the undercoolings listed above. In practice, the parameters listed in Table 1 for Figs. 12–15 show that the temperature variation between two adjacent cell layers is typically of $G \times l_{CA} = 0.03$ K, hence good convergence of the simulation is verified.

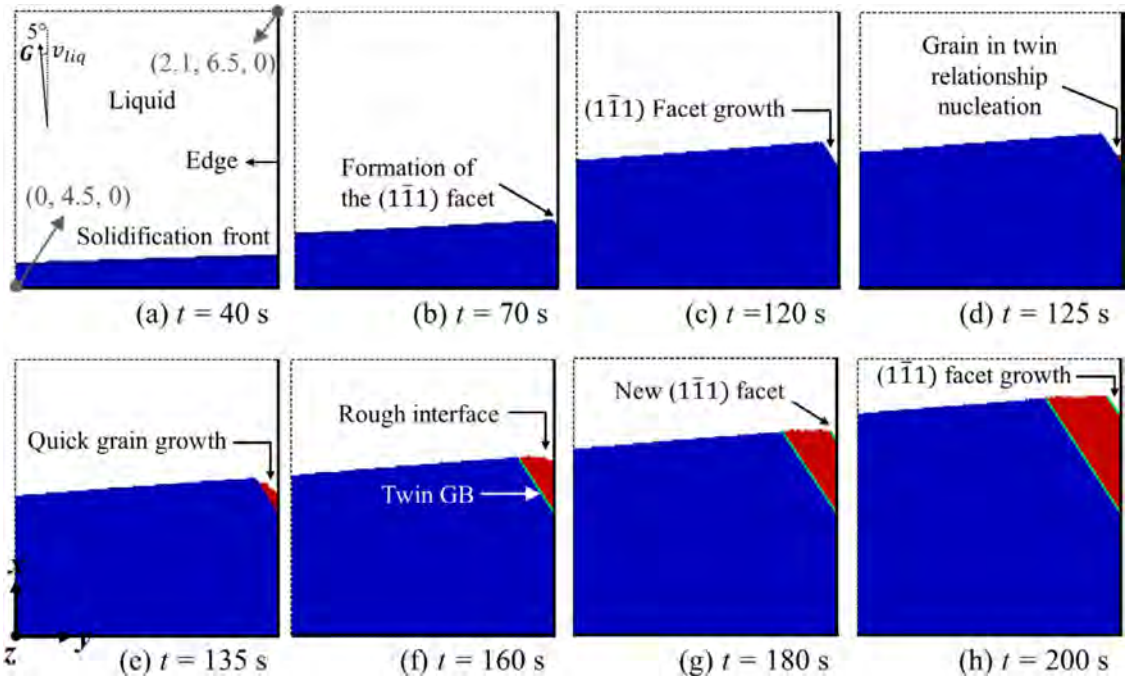

Fig. 12. 3D CA computations showing (a) growth of a solidification front from an initial seed, (b) formation of a (1$\bar{1}$1) facet, (c) growth of the facet, (d) nucleation of a grain in twin relationship at the bottom of the facet, (e) quick twin growth along the (1$\bar{1}$1) facet defining the twin grain boundary, (g) twin growth and formation of a new (1$\bar{1}$1) facet and (h) growth of the new (1$\bar{1}$1) facet. The blue and red grains are in Σ3 twin relationship. Coordinates of the bottom-left and top-right corners are given in *mm*. See Table 1 for simulation parameters.

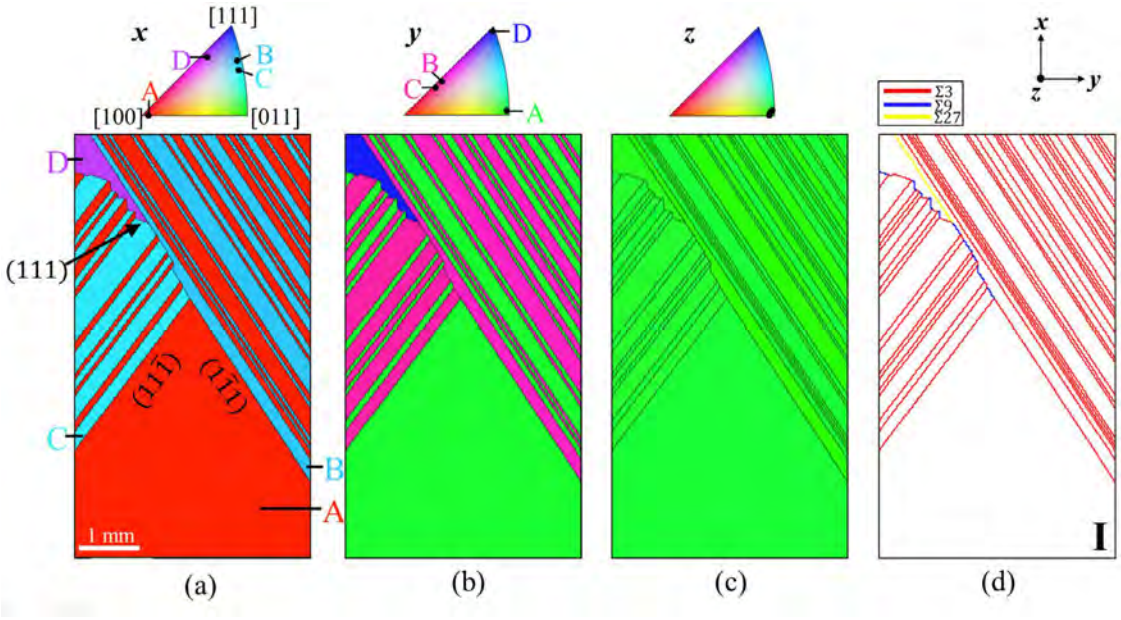

Fig. 13. 3D CA computation results of the directionally solidified grain structure for comparison with the experiment counterpart in Fig. 3. The (a) longitudinal direction of the sample, x (also growth direction), (b) transverse direction of the sample, y, and (c) normal direction to the sample, z, are projected in the frame made of the measured {[100], [010], [111]} crystallographic directions and represented using the color code of the IPF. They are of A-, B-, C- and D-type. The CSL map characterizing the grain boundary relationships is shown in (d) with twin boundaries Σ3, Σ9 and Σ27. The D-type grain is the result of nucleation in twin relationship on a (111) facet of a C-type grain at a faceted/faceted groove formed with a B-type grain. This computation result is labeled I in (d) for comparison with results in Fig. 14. See Table 1 for simulation parameters.

Fig. 12 shows a 3D CA simulation with a complete twinning sequence. It starts from the formation of a {111} facet activation at the sample edge. The identified twinning plane is the (1$\bar{1}$1) plane. The local undercooling at the bottom of the facet increases with time as the facet develops in a constant temperature gradient and the rough part of the interface remains at the same undercooling. Consequently, at time 125 s, the nucleation undercooling $\Delta T^{E}_{N,T}$ is reached and a grain in twin relationship is formed. With initial seed of Euler angles (356°, 44°, 3°), the grain in Σ3 twin relationship with facet (1$\bar{1}$1) takes Euler angles (–21.3°, 89.7°, 47.3°) as computed by Eq. (6). The new grain quickly grows to catch up with the s/l interface. It keeps growing, the twin relationship between the two grains being maintained with a fixed grain boundary. During growth of the grain in twin relationship, it is worth noticing that the grain does not form the common (1$\bar{1}$1) facet right after its nucleation. The facet forms afterwards at 180 s when the activation undercooling for the grain in twin relationship is reached in Fig. 12(g). The latter facet then starts growing and the local undercooling at its bottom increases. A second grain in twin relationship is nucleated after 200 s (not shown in Fig. 12), which naturally adopts the crystallographic orientation of the initial seed due to a second Σ3 operation from a similar (1$\bar{1}$1) facet but from the first grain in twin relationship. This is repeated

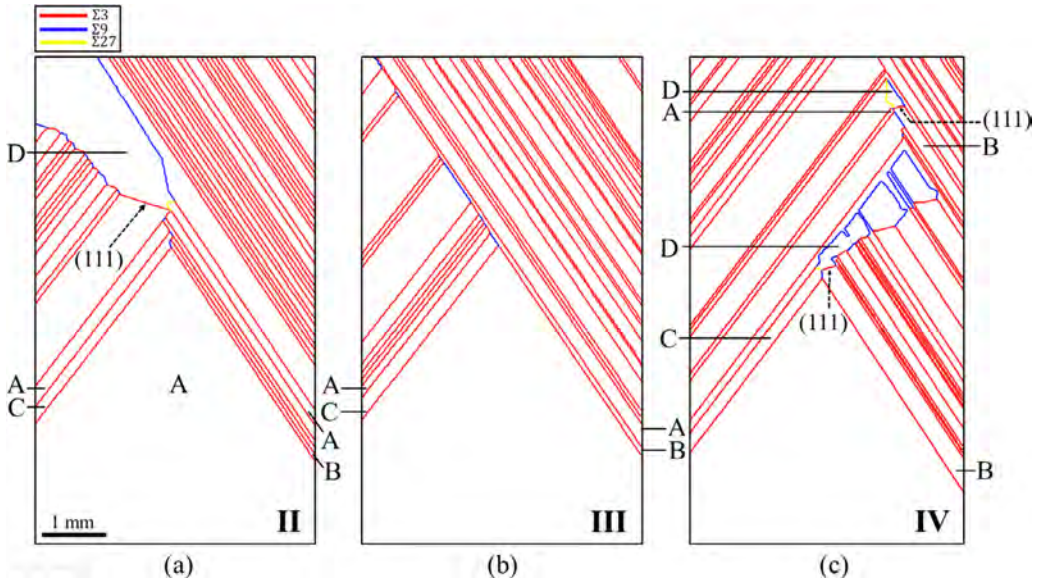

Fig. 14. 3D CA computation results of directionally solidified grain structure. CSL maps are shown for 3 simulations labeled II, III and IV for comparison with simulation labeled I in Fig. 13(d). Differences come from the random process used to determine the activation undercooling of the {111} facets of the grains. Occurrence of the nucleation of grain D depends on different mechanisms: (a) twin nucleation on a (111) facet of grain C at a faceted/faceted groove formed with grain A, (b) no twin nucleation occurred so grains A, B and C are present and grain boundaries are only of Σ3 and Σ9 types, (c) grain E results from nucleation on a (111) facet of grain A at a faceted/faceted groove with grain C, twice. See Table 1 for simulation parameters.

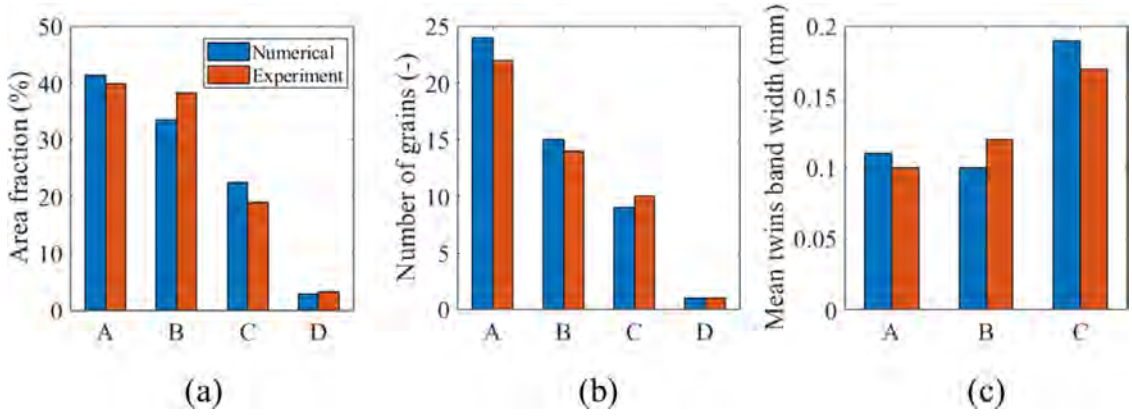

Fig. 15. Statistical analyzes showing (a) the area fraction, (b) the number of grains and (c) the mean band width between twin boundaries for the simulation results in Fig. 13 considering grains A, B, C and D (in blue). The same analyzes with experimental observations shown in Fig. 3 are given for comparison in red. See Table 1 for simulation parameters.

several times during the simulation similarly to the experiments displayed in Fig. 3. The result of such successive twinning events is shown on the RHS of Figure 13 at a larger scale after complete solidification of the sample, i.e. at 700 s. The LHS and RHS grains in Fig. 12 are of crystallographic orientation labelled A and B in Fig. 13, respectively.

4.3. Grain structure of the fully solidified sample

Color maps in Fig. 13(a-c) are based on the IPF scale displayed above each image. They are the same as those used in Fig. 3. The same colors are also used to draw the twin relationships in the CSL maps of Fig. 13(d) and 3(d) [48]. The simulated results can thus be directly compared with the experimental ones. As can be seen, the general trends agree well. This not only concerns the generation of grains in twin relationship on the RHS boundary of the sample, but also on its LHS boundary due to the formation of a $(11\overline{1})$ facets from the seed (grain A). The two sets of $\Sigma 3$ twin relationships with a common $(1\overline{1}1)$ plane on the RHS (A/B type grain boundaries) and $(11\overline{1})$ plane on the LHS (A/C type grain boundaries) are made of grains with various band widths. The band width is directly controlled by the values of the mean undercooling, $\Delta T_{g,m}^{\{111\}}$, and standard deviation, $\Delta T_{g,s}^{\{111\}}$, defined to activate the {111} facets. For instance, for a given value of the mean undercooling, a larger value of the standard deviation creates a broader variation of the band widths (more irregular arrangement of the twins). A detailed parametric study can be found in Reference 49.

Unlike grains of B-type and C-type, the grain labelled D nucleated in the bulk at a faceted/faceted groove on a (111) plane of a C-type grain. The $\Sigma 9$ twin boundaries are observed whenever B-type and C-type or D-type and A-type grains meet, whereas a $\Sigma 27$ twin boundary originates from D-type and B-type. These are simply the consequences of s/l interface encounters during growth of A-, B-, C- and D-type grains. These results are consistent with the experimental results (Fig. 3). A single grain D forms in Fig. 13. Prior to its nucleation, a total of 5 grooves between B-type and C-type grains were formed but did not lead to nucleation of the D-type grain on the (111) plane of a C-type grain. Two reasons can explain the delay in nucleating grain D. First, a groove with a (111) facet on a C-type grain could have formed but its undercooling did not reached the nucleation threshold for a twin grain, $\Delta T_{N,T}^{B}$, prior the competing neighboring grain hindered its growth. Second, the current activation undercooling for {111} faceted interfaces did not allow formation of the groove. As a result of this analysis, it is clear that the distribution of activation undercooling plays a key role in controlling the simulated grain structure. It renders the different nucleation undercoolings of the {111} facets during growth. This undercooling can be modified by the presence of impurities, defects like dislocations and local accumulation of crystal deformation [4].

The typical computational time for the simulation shown in Fig. 13 does not exceed 30 minutes on a single CPU. Consequently, while maintaining the same values of the mean and standard deviation of the activation undercooling, the 3D CA model can be used for a statistical study. This is simply done by doing the same simulation several times and comparing the results. Because the sequence of random numbers differs at each simulation, sampling of the activation undercooling of the eight {111} facets for each newly created grain varies and several results are obtained. The first simulation, labelled I in Fig. 13(d), can be compared with 3 additional simulation cases labelled II, III and IV shown in Figure 14. As can be seen by comparing the CSL maps of Fig. 14 with the experimental map in Fig. 3 (d), larger differences are observed with cases II to IV against case I shown in Fig. 13(d). In case II (Fig. 14(a)), grain D nucleated in the bulk, on the (111) facet of grain C, but as part of a groove formed with a A-type grain. However, the A-type grain did not survive growth competition with grain D and the latter entered in competition with a B-type grain, resulting in a large $\Sigma 9$ twin grain boundary. In case III (Fig. 14(b)), no nucleation in the bulk occurred. As explained above, this is either due to the fact that a grain boundary groove with at least one {111} facet formed between C- and B-type grains but did not survive competition before the nucleation undercooling condition $\Delta T_{N,T}^{B}$ was reached, or because of no {111} facet formed at all between C- and B-type grains yet in growth competition. The reader should yet note that this configuration did not often happen in the present simulations, i.e. at least one nucleation in the bulk is usually observed. Finally, case IV (Fig. 14(c)) shows another configuration. Two nucleation events of grains in twin relationship took place in the bulk. Both of them correspond to nucleation of a grain in a $\Sigma 3$ relationship on a (111) plane of a B-type grain. The first twin nucleation event occurred in a groove formed by B- and C-type grains, the second in a groove defined by B- and A-type grains. The grain is labelled E as its crystallographic orientation slightly differs from grain D.

Quantitative comparisons between simulation and experiments are summarized in Figure 15. They concern the area fraction, the number of grains of types A–D and the mean twin band width of grains of type A–C. For a given grain, the latter is defined by the width between two twinning events of a given grain type in a direction perpendicular to the twinning planes. Only simulation I (Fig. 13) is used in Fig. 15 as it reflects best the twinning mechanisms observed in the experiment. The area of the initial seed is not considered when computing the grain area fraction since we focus on the grains that formed as a result of nucleation events. This is why for band width computations, only edge twin nucleation is considered. One can notice the overall good agreement in computation I with

Table 2
Area fraction, number and mean band width for grains defined by their common crystal orientation A, B, C, D and E, considering simulations (I–IV) shown in Figs 13 and 14 as well as the experimental grain structure shown in Fig. 3.

	Orientation or grain type	Experiment Fig.3	Simulations Fig. 13 I	Fig. 14 II	Fig. 14 III	Fig. 14 IV
Area fraction (%)	A	39.8	41.3	43.4	52.4	44.3
	B	38.1	33.4	23.5	31.1	22.2
	C	18.9	22.4	18.9	16.5	29.1
	D	3.2	2.9	13.8	0	0
	E	0	0	0	0	4.5
Number	A	22	24	24	21	26
	B	14	15	16	14	16
	C	10	9	9	7	11
	D	1	1	1	0	0
	E	0	0	0	0	2
Mean band width (mm)	A	0.10	0.11	0.15	0.12	0.13
	B	0.12	0.10	0.09	0.13	0.13
	C	0.17	0.19	0.16	0.15	0.18

experimental observations. Area fraction of A-type grains obtained in the simulation (41,3%) is very close to the area fraction measured in the experiment (39,8%). The number of grains in the computation is higher (24) than the one in the experiment (22) nevertheless clearly of the same order of magnitude, the mean band width is quantitatively comparable, 0.10 mm in the experiment and 0.11 mm in the simulation. For B-type grains, the area fraction is 4,7% lower in the simulation (33.4%) than in the experiment (38.1%). The number of grains is almost identical and the mean band width in the simulation is lower (0.1 mm) compared to the experiment (0.12 mm). One can apply a similar reasoning for C-type grains.

Table 2 summarizes the quantitative parameters defined above for the experimental observations and all the simulation results presented in this work (I–IV). Configuration of simulation II (Fig. 14(a)) is very similar to configuration of simulation I. As detailed above, grain D nucleated in the bulk on the (111) facet of a C-type grain. This nucleation occurred early when compared to simulation I which thus explains the larger area fraction of grain D, i.e. 13.8% for simulation II and 2.9% for simulation I. The same reason explains the lower values of area fraction of C-type grains in the simulation II (18.9%) compared to simulation I (22.4%). One can expect a similar observation for A, i.e. the early nucleation of grain D would also prevent the growth of A-type grains, especially in the left part of the domain. However, area fraction of A-type grains in simulation II is higher (43.4 %) than in simulation I (41,3 %). This is explained by the larger mean band width of A-type grains in simulation II (0.142 mm) compared to simulation I (0.102 mm). In simulation III (Fig. 14(b)), no nucleation in the bulk is observed, and twin nucleation events only occur on the edges on the domain. One can note a large area fraction of A-type grains, i.e. 52.42 %, its growth being unaffected by any nucleation in the bulk. Hence, one would also expect a larger area fraction of C-type grains. However, the obtained value (16.5 %) is lower than that in simulations I and II. This is due to the low mean band width (0.15 mm) and lower number (7) of C-type grains. Results of simulation IV (Fig. 14(c)) are also similar to simulations I and II, although growth of grain E was directed towards the right part of the simulation domain as it nucleated on a {111} facet of a B-type grain (C-type grains in simulations I and II). Consequently, grain E does not compete as much with C-type grains, resulting in a larger area fraction of C-type grains (29.1%) compared to simulations I and II (22.4% and 18.9%, respectively) as well as a higher number of C-type grains, 11 (compared to 9 for both simulations I and II). Similarly, since grain E grows towards the right part of the domain, it prevents the growth of B-type grains, resulting in a lower area fraction (22.2%) for simulation IV compared to simulations I and II (33.4% and 23.5%, respectively).

5. Conclusions

A 3D CA model is introduced for solidification of silicon polycrystalline grain structures. Special attention is taken to model the formation of grains in $\Sigma 3$ twin relationship as they typically constitute 50% of the grain boundaries [7,8] and drive the formation of all other grain and twin boundaries formed during growth [3,4]. Thanks to in-situ X-ray imaging using the GaTSBI device [14,15], the mechanisms for the formation of grains in twin relationship upon crystallization of silicon were revealed and described [3,40–42]. Several observations are thus available that could be compared with simulations. The simulations in the paper reach the following objectives:

- Planar morphology of a rough s/l interface is simulated with all grains growing at a single undercooling upon stationary directional solidification.
- Formation of {111} facets is modeled by a CA growth algorithm, where the Cartesian equation of each facet is defined for a given grain. Facets are created when the s/l interface reaches an activation undercooling. This parameter is randomly chosen using a Gaussian distribution. The growth velocity of the facets is imposed based on experimental measurements. A conditioned CA capture algorithm is defined to model faceted growth. It is also demonstrated the rough-to-faceted transition can be modeled.
- Dedicated algorithms to nucleate and grow new grains in twin relationship with their existing neighboring grains developing {111} facets are defined. The nucleation is subjected to reaching a nucleation undercooling. Different values for such undercooling are used, depending if the facet is formed at sample edge or at a grain boundary groove, as measured by X-ray imaging [42].
- Directional solidification of bi-crystals forming faceted/faceted or rough/faceted grooves with the liquid reproduce well the s/l interface morphology and the resulting grain boundary orientation.
- Formation of twin grains at sample edges are compared with observations. The main parameter to obtain satisfactory results is the nucleation activation of the {111} facets.
- An EBSD map is finally derived from the 3D simulated grain structure and compared with its counterpart produced on a fully solidified sample using GaTSBI [42,4]. Quantitative comparisons consider the area fraction as well as the number and mean band width of regions produced by successive twinning while starting from a single seed with known orientation. Results are discussed based on the different nucleation planes that could be activated. CSL maps are also produced and compared with the measurements, revealing the $\Sigma 3$, $\Sigma 9$ and $\Sigma 27$ twin relationships between grains.

A major advantage of the CA method compared to phase field simulations and other methods proposed in the literature is the computational time [16–21]. It can thus be anticipated that the CA method is suitable to optimize the grain structure produced during crystallization of silicon at the processing scale including the crucial modeling of twin nucleation.

Declaration of Competing Interest

The authors declare that they have no known competing financial interests or personal relationships that could have appeared to influence the work reported in this paper.

Acknowledgements

The present work was funded by the project CrySaLID (ANR-14-CE05-0046-01) of the French National Research Agency (ANR). Laurent Barrallier and Fabrice Guittonneau from Arts et Métiers ParisTech (Aix-en-Provence, FR) are greatly acknowledged for the EBSD measurements.

References

[1] J.S. Lacerda, J.C. v. d. Bergh, Diversity in solar photovoltaic energy: Implications for innovation and policy, Renewable and Sustainable Energy Reviews 54 (2016) 331–340.

[2] M. Trempa, C. Reimann, J. Friedrich, G. Müller, A. Krause, L. Sylla, T. Richter, Defect formation induced by seed-joints during directional solidification of quasi-mono-crystalline silicon ingots, Journal of Crystal Growth 405 (2014) 131–141.

[3] M.G. Tsoutsouva, T. Riberi-Béridot, G. Regula, G. Reinhart, J. Baruchel, F. Guittonneau, L. Barrallier, N. Mangelinck-Noël, In situ investigation of the structural defect generation and evolution during the directional solidification of ⟨110⟩ seeded growth Si, Acta Materialia 115 (2016) 210–223.

[4] T. Riberi-Béridot, M.G. Tsoutsouva, G. Regula, G. Reinhart, F. Guittonneau, L. Barrallier, N. Mangelinck-Noël, Strain building and correlation with grain nucleation during silicon growth, Acta Materialia 177 (2019) 141–150.

[5] K. Kakimoto, Crystallization of Silicon by a Directional Solidification Method, in: Kazuo Nakajima, Noritaka Usami (Eds.), Crystal Growth of Si for Solar Cells, Springer, Berlin Heidelberg, 2009, pp. 55–69.

[6] C.-W. Lan, C. Hsu, K. Nakajima, Multicrystalline Silicon Crystal Growth for Photovoltaic Applications, in: P. Rudolph (Ed.), Handbook of Crystal Growth, Second EditionElsevier, Boston, 2015, pp. 373–411.

[7] A. Voigt, E. Wolf, H.P. Strunk, Proc 14th Europ, PV Solar Energy Conf., Barcelona, 1997, pp. 774–777. 30th June-4th July.

[8] A. Voigt, E. Wolf, H.P. Strunk, Grain orientation and grain boundaries in cast multicrystalline silicon, Material Science and Engineering B 54 (1998) 202–206.

[9] P.D. Bristowe, in: R. Hull (Ed.), EMIS, 1999 299308.

[10] K.A. Jackson, Constitutional supercooling surface roughening, Journal of Crystal Growth 264 (2004) 519–529.

[11] T. Duffar, Comprehensive review on grain and twin structures in bulk photovoltaic silicon, Recent Research Development in Crystal Growth 5 (2010) 61–111.

[12] T. Ribéri-Béridot, N. Mangelinck-Noël, A. Tandjaoui, G. Reinhart, B. Billia, T. Lafford, J. Baruchel, L. Barralier, On the impact of twinning on the formation of the grain structure of multi-crystalline silicon for photovoltaic applications during directional solidification, Journal of Crystal Growth 418 (2015) 38–44.

[13] B. Ryningen, G. Stokkan, M. Kivambe, T. Ervik, O. Lohne, Growth of dislocation clusters during directional solidification of multicrystalline silicon ingot, Acta Materialia 59 (2011) 7703–7710.

[14] A. Tandjaoui, N. Mangelinck-Noël, G. Reinhart, J.-J. Furter, B. Billia, T. Lafford, J. Baruchel, X. Guichard, Real time observation of the directional solidification of multicrystalline silicon: X-ray imaging characterization, Energy Procedia 27 (2012) 82–87.

[15] A. Tandjaoui, N. Mangelinck-Noël, G. Reinhart, B. Billia, X. Guichard, Twinning occurrence and grain competition in multi-crystalline silicon during solidification, Comptes Rendus Physique 14 (2013) 141–148.

[16] H.K. Lin, C.W. Lan, Three-dimensional phase field modeling of silicon thin-film growth during directional solidification: Facet formation and grain competition, Journal of Crystal Growth 401 (2014) 740–747.

[17] J.W. Jhang, C.W. Lan, Three-dimensional phase field modelling of twin nucleation during directional solidification of multi-crystalline silicon, Journal of Crystal Growth 520 (2019) 33–41.

[18] W. Miller, A. Popescu, G. Cantù, Solidification of multycristaline silicon−simulation of micro-structures, Journal of Crystal Growth 385 (2014) 127–133.

[19] A. Nadri, Y. Duterrail-Couvat, T. Duffar, Two-dimensional numerical modeling of grain structure in multi-cristalline silicon ingot, Journal of Crystal Growth 385 (2014) 16–21.

[20] B. Wu, S. Scott, N. Stoddard, R. Clark, A. Sholapurwalla, Simulation of silicon casting process for photovoltaic (PV) application, in: Proceedings of the 2009 TMS Annual Meeting & Exhibition.

[21] X. Qi, L. Liu, T. Riberi-Béridot, N. Mangelinck-Noël, W. Miller, Simulation of grain evolution in solidification on meso-scopic scale, Comput. Mater. Sci. 159 (2019) 432–439.

[22] Ch.-A. Gandin, M. Rappaz, A coupled finite element-cellular automaton model for the prediction of dendritic grain structures in solidification processses, Acta Metallurgica and Materialia 42 (1994) 2233–2246.

[23] T. Carozzani, H. Digonnet, Ch.-A. Gandin, 3D CAFE modeling of grain structures: Application to primary dendritic and secondary eutectic solidification, Modeling and simulation in materials science and engineering 20 (2012) 015010.

[24] H. Takatani, Ch.-A. Gandin, M. Rappaz, EBSD characterisation and modelling of columnar dendritic grains growing in the presence of fluid flow, Acta materialia 48 (2000) 675–688.

[25] G. Guillemot, Ch.-A. Gandin, H. Combeau, Modeling of macrosegregation and solidification grain structures with a coupled cellular automaton - Finite element model, ISIJ International 46 (2006) 880–895.

[26] G. Guillemot, Ch.-A. Gandin, M. Bellet, Interaction between single grain solidification and macrosegregation: Application of a cellular automaton-finite element model, Journal of crystal growth 303 (2007) 58–68.

[27] A. Saad, Ch.-A. Gandin, M. Bellet, N. Shevchenko, S. Eckert, Simulation of Channel Segregation During Directional Solidification of In—75 wt pct Ga - Qualitative Comparison with In Situ Observations, Metallurgical and materials transactions A 46 (2015) 4886–4897.

[28] T. Carozzani, Ch.-A. Gandin, H. Digonnet, M. Bellet, K. Zaidat, Y. Fautrelle, Direct Simulation of a Solidification Benchmark Experiment, Metallurgical and materials transactions A 44 (2013) 873–887.

[29] G. Reinhart, Ch.-A. Gandin, N. Mangelinck-Noël, H. Nguyen-Thi, J.-E. Spinelli, J. Baruchel, B. Billia, Influence of natural convection during upward directional solidification: a comparison between in situ X-ray radiography and direct simulation of the grain structure, Acta materialia 61 (2013) 4765–4777.

[30] T.-T.-M. Nguyen, Ch.-A. Gandin, H. Combeau, M. Zaloznik, M. Bellet, Finite element multi-scale modelling of chemical segregation in steel solidification taking into account the transport of equiaxed grains, Metallurgical and materials transactions A 49 (2018) 1725–1748.

[31] Ch.-A. Gandin, M. Rappaz, R. Tintillier, Three-dimensional probabilistic simulation of solidification grain structures: application to superalloy precision castings, Metallurgical transactions 24A (1993) 467–479.

[32] Ch.-A. Gandin, M. Rappaz, R. Tintillier, 3-Dimensional simulation of the grain formation in investment castings, Metallurgical transactions 25A (1994) 629–635.

[33] Ch.-A. Gandin, M. Rappaz, A 3D cellular automaton algorithm for the prediction of dendritic grain growth, Acta materialia 45 (1997) 2187–2195.

[34] S. Chen, G. Guillemot, Ch.-A. Gandin, 3D CAFE modeling for solidification grain structures in GTAW, ISIJ international 54 (2014) 401–407.

[35] S. Chen, G. Guillemot, Ch.-A. Gandin, Three-dimensional cellular automaton-finite element modeling of solidification grain structures for arc-welding processes, Acta materialia 115 (2016) 448–467.

[36] Y. Lian, S. Lin, W. Yan, W.K. Liu, G.J. Wagner, A parallelized three-dimensional cellular automaton model for grain growth during additive manufacturing, Computational Mechanics 61 (2018) 543–559.

[37] J.A. Koepf, M.R. Gotterbarm, M. Markl, C. Körner, 3D multi-layer grain structure simulation of powder bed fusion additive manufacturing, Acta Materialia 152 (2018) 119–126.

[38] Y. Lian, Z. Gan, C. Yu, D. Kats, W.K. Liu, G.J. Wagner, A cellular automaton finite volume method for microstructure evolution during additive manufacturing, Materials & Design 169 (2019) 107672.

[39] T. Duffar, C.T. Nwosu, I.M. Asuo, J. Muzy, N.D.Q. Chau, T. Du Terrail-Couvat, F. Robaut, Experimental study of grain boundary orientations in multi-crystalline silicon, Journal of Crystal Growth 401 (2014) 404–408.

[40] A. Tandjaoui, N. Mangelinck-Noël, G. Reinhart, B. Billia, T. Lafford, J. Baruchel, Investigation of grain boundary grooves at the solid-liquid interface during directional solidification of multi-crystalline silicon: in-situ characterization by X-ray imaging, Journal of Crystal Growth 377 (2013) 203–211.

[41] K.-K. Hu, K.-I. Maeda, H. Morito, K. Shiga, In situ observation of grain-boundary development from a facet-facet groove during solidification of silicon, Acta Materialia 153 (2018) 186–192.

[42] V. Stamelou, M.G. Tsoutsouva, T. Riberi-Béridot, G. Reinhard, G. Regula, J. Baruchel, N. Mangelinck-Noël, {111} facet growth laws and grain competition during silicon crystallization, Journal of Crystal Growth 479 (2017) 1–8.

[43] H.-J. Bunge, in Texture analysis in materials science Butterworth & Co (1982).

[44] A. Pineau, G. Guillemot, D. Tourret, A. Karma, Ch.-A. Gandin, Growth competition between columnar dendritic grains – Cellular automaton versus phase field modeling, Acta Materialia 155 (2018) 286–301.

[45] T. Riberi-Béridot, M.G. Tsoutsouva, G. Regula, G. Reinhard, I. Périchaud, J. Baruchel, N. Mangelinck-Noël, Growth undercooling in multi-crystalline pure silicon and in silicon containing light impurities (C and O), J. Cryst. Growth 466 (2017) 64–70.

[46] Ch.-A. Gandin, From constrained to unconstrained growth during directional solidification, Acta Materialia 48 (2000) 2483–2501.

[47] A. de Bussac, Ch-A. Gandin, Prediction of a process window for the investement casting of dendritic single crystals, Materials Science and Engineering A 237 (1997) 35–42.

[48] R. Hielscher, H. Schaeben, A novel pole figure inversion method: Specification of the MTEX algorithm, Journal of Applied Crystallography 41 (2008) 1024–1037.

[49] A. Pineau, Modélisation 3D de structures de grains par une approche automate cellulaire. Application à la compétition de croissance dendritique et à la cristallisation du silicium polycristallin. PhD thesis. PSL University MINES ParisTech, 2019.